



저작자표시-비영리-변경금지 2.0 대한민국

이용자는 아래의 조건을 따르는 경우에 한하여 자유롭게

- 이 저작물을 복제, 배포, 전송, 전시, 공연 및 방송할 수 있습니다.

다음과 같은 조건을 따라야 합니다:



저작자표시. 귀하는 원저작자를 표시하여야 합니다.



비영리. 귀하는 이 저작물을 영리 목적으로 이용할 수 없습니다.



변경금지. 귀하는 이 저작물을 개작, 변형 또는 가공할 수 없습니다.

- 귀하는, 이 저작물의 재이용이나 배포의 경우, 이 저작물에 적용된 이용허락조건을 명확하게 나타내어야 합니다.
- 저작권자로부터 별도의 허가를 받으면 이러한 조건들은 적용되지 않습니다.

저작권법에 따른 이용자의 권리는 위의 내용에 의하여 영향을 받지 않습니다.

이것은 [이용허락규약\(Legal Code\)](#)을 이해하기 쉽게 요약한 것입니다.

[Disclaimer](#)

의학박사 학위논문

The radiomics score from DCE–
MRI predicts a high–risk group in
glioblastoma patients
independently of IDH mutation
status

교모세포종 환자에서의 역동적 조영증강 자기공명
영상의 라디오믹스 점수를 이용한 IDH 돌연변이
상태 독립적 고위험군 예측 연구

2021년 8월

서울대학교 대학원
의학과 영상의학전공

PAK ELENA

The radiomics score from DCE-MRI predicts a high-risk group in glioblastoma patients independently of IDH mutation status

지도 교수 최승홍

이 논문을 의학박사 학위논문으로 제출함
2021년 4월

서울대학교 대학원
의학과 영상의학전공
PAK ELENA

PAK ELENA의 의학박사 학위논문을 인준함
2021년 7월

위원장	_____
부위원장	_____
위원	_____
위원	_____
위원	_____

Abstract

The radiomics score from DCE–MRI predicts a high–risk group in glioblastoma patients independently of IDH mutation status

Pak Elena
Department of Medicine
The Graduate School
Seoul National University

Objective

To develop a radiomics risk score based on dynamic contrast–enhanced (DCE) MRI for the prediction high–risk group in glioblastoma patients.

Materials and Methods

One hundred fifty patients (92 men (61.3%); mean age, 60.5 ± 13.5 years) with glioblastoma who underwent a preoperative MRI were enrolled in the study. Six hundred forty–two radiomic features were extracted from K^{trans} , V_p and V_e maps of DCE MRI, where regions of interest were based on both non–enhancing T2 hyperintense areas and T1–weighted contrast–enhancing areas. Using feature selection algorithms, significant radiomic features were selected. Subsequently, a radiomics risk score was developed using a weighted combination of the selected features in the discovery set ($n = 105$) and validated in the

validation set (n = 45) by investigating the difference in prognosis between “radiomics risk score” groups. Finally, a multivariate Cox–regression for 1–year progression–free survival was performed using the radiomics risk score and clinical variables.

Results

Sixteen radiomic features obtained from non–enhancing T2 hyperintense areas were selected out of 642 features. The radiomics risk score stratified high– and low–risk groups in both the discovery and validation set in log rank test (both $p < 0.001$). The radiomics risk score increased the risk of progression in glioblastoma patients, independently of IDH–mutation status (HR = 3.56, $p = 0.004$; HR = 0.34, $p = 0.022$, respectively).

Conclusion

We developed and assessed the “radiomics risk score” from the features of DCE MRI based on non–enhancing T2 hyperintense areas for risk stratification of progression at 1 year in glioblastoma patients, which was independent of IDH mutational status.

.....

keywords : Glioblastoma, progression, dynamic contrast–enhanced MRI, K^{trans} , V_e , V_p , radiomics

Student Number : 2018–39720

Table of Contents

Introduction.....	4
Materials and methods.....	14
Results	23
Discussion.....	27
References.....	34
Tables	52
Figures	58
Supplementary materials.....	71
Abstract in Korean	90

Introduction

Gliomas are a general term which describes primary brain tumors [1]. They are classified into four grades based on histology. Grade I and grade II gliomas referred to as low-grade gliomas, are less aggressive tumors with a slow growth rate and a better prognosis [2]. On the other hand, high-grade gliomas (grade III and grade IV) are more aggressive tumors [2], which causes deterioration of the life quality [3].

About 60% of all high-grade gliomas are glioblastomas with an annual incidence of over 3 per 100,000 [2]. It often begins around 64 years and glioblastoma is more common in men [4]. It is an aggressive brain tumor with a high recurrence rate. Median survival and 5-year survival after multi-modality treatment is reported to be approximately 15 months [5] and less than 7% [6], respectively. The multimodal glioblastoma treatment protocol consists of maximum possible surgical resection, followed by radiation therapy with concurrent temozolomide and 6 cycles of adjuvant temozolomide [7]. The median time to progression is about 6.9 months with >90% of glioblastoma recurring at the baseline [8]. Several genes are important to the understanding of glioblastoma prognosis [9]. The O⁶-methylguanine-DNA methyltransferase (MGMT) promoter methylation and isocitrate dehydrogenase gene 1 and 2 (IDH1/2)

mutations have been associated with a favorable prognosis[10].The cellular DNA repair enzyme of MGMT removes alkyl groups from the O⁶ position of guanine, thereby counteracting the effect of alkylating drugs, such as temozolomide[11]. About 30–40% of glioblastomas have methylated MGMT [12]. The MGMT promoter methylation is associated with prolonged survival[13]. Previous research showed that the MGMT promoter methylation status was a predictive biomarker for benefit from the addition of temozolomide[14].

Glioblastomas are highly vascularized tumors associated with high vascular permeability, which can then lead to edema and angiogenesis[15]. The blood–brain barrier (BBB) defends the normal microenvironment of the central nervous system[16]. It is formed by 3 cellular elements, the astrocyte end–feet, pericytes and BBB endothelial cells[17]. Pericytes are important in angiogenesis, formation of endothelial tight junctions, structural integrity and differentiation of the vessel[17]. The BBB endothelial cells are characterized by the lack of fenestrations, rare pinocytic vesicular transport, and more extensive tight junctions[17]. When glioma aggravates, BBB becomes disrupted and normal vessel endothelial cells are roughly separated from the main vascular structure, forming new angiogenic spots. They migrate when

forming new vessels and destroy normal vessel structure to arrive at the tumor [18]. Besides tumors secrete a lot of different molecules that change the normal microenvironment [18]. In glioblastoma, the morphological changes of blood vessels include disruption of tight junctions and the formation of fenestrations. In addition, the basal lamina thickness is changed and the width of the perivascular space is increased along with the number of pericytes related to the vessels [18]. Therefore, the microvascular leakage of the tumor might be important in tumor grade and prediction of prognosis [19].

Magnetic resonance imaging (MRI) is a medical imaging technique that enables the diagnosis of glioblastoma, assessment of the therapeutic response, and monitoring of the disease progression [20]. In addition, MRI can directly image biochemical changes in the tumor and surrounding tissue [21]. High-field MRI is commonly used in patients with disorders of the brain, including gliomas [22]. 3T MRI has a higher sensitivity in diagnosing the brain tumor, as compared with 1.5T MRI [23].

Using gradient echo allows to reduce the MRI examination time, which in turn leads to the decrease in motion artifact [24]. This imaging technique is based on only a single RF pulse with readout gradient reversal [25] and without a 180° refocusing pulse [24]. To improve the

image contrast, the flip angle was decreased under 90° in single-slice acquisition [24]. Consequently, gradient echo sequence enables the acquisition of high quality images with fewer artifacts in a shorter duration [24]. Bagley et al. demonstrated that magnetic susceptibility artifacts on T2*-weighted gradient echo MRI seems to be useful in the preoperative assessment of gliomas [26].

A T2 weighted fluid-attenuated inversion recovery (FLAIR) is an inversion recovery technique with a long inversion time (TI), echo time (TE) and repetition time (TR). This sequence removes signals from the cerebrospinal fluid effectively (CSF) [27]. Some previous studies focused on the perfusion or permeability parameters from non-enhancing T2 high signal intensity (SI) for prognosis prediction in patients with glioblastoma [28,29].

A T1-weighted images are used for depicting normal anatomy and can highlight pathological abnormalities if used with a contrast agent [30]. This sequence is acquired with short TE and TR [31]. For contrast enhancement, paramagnetic substances (usually gadolinium) which shortened the T1 relaxation time of surrounding protons are commonly used [31]. The enhancement of contrast is explained by two main mechanisms: contrast leakage through the damaged BBB and/or high

vascularization inside pathological lesion[31].

Conventional MRI helps evaluate the anatomical and structural lesion details, but its specificity is limited. Recently, there have been improvements in contrast resolution with improved contrast agents and higher magnetic field strengths; however, tissue characterization using conventional MRI is still limited [32]. Contrarily, advanced MRI techniques, such as perfusion imaging, spectroscopy imaging, and diffusion imaging, can give additional information on tumor tissue in addition to morphological imaging [33].

Perfusion is a biological process that relates to the delivery of nutrients and oxygen to a capillary bed in tissue [34]. Perfusion MRI technique has been used to assess the tissue vascularization, in vivo tumor microcirculation and angiogenesis [35]. Dynamic susceptibility contrast (DSC)–MRI and dynamic contrast–enhanced (DCE)–MRI are perfusion MRI sequences using exogenous contrast agents [34].

The DSC–MRI is based on T_2/T_2^* –weighted sequences [36]. The contrast agent used for this technique is supposed to be mostly limited to the vascular space, which gives the useful information about perfusion (the blood flow, blood volume, and transit time) [37]. Recent research showed that DSC–MRI techniques have higher sensitivity in

differentiating progressive disease from pseudoprogression in patients with glioblastoma [38].

The DCE–MRI has been widely used in clinical practice, where multiphase MRI scans are acquired after intravenous injection of a contrast agent [37]. It focuses on the measurement of the density, integrity and “permeability imaging” or leakiness of tissue vasculature, which can provide additional information to the vascularity. The DCE–MRI is based on mathematical models and measurements of how a tracer perfuses through the vessels [39]. Because of vascular permeability and BBB disruption in gliomas, the contrast agent, which was administered intravenously, leaks easily from intravascular compartment to extravascular extracellular space (EES), leading to an increase in T1 signal intensity [40]. Vessels in the normal tissue may be described by a range of parameters which measure vessel blood flow, tissue volume fractions, and permeability [39]. DCE–MRI can fully demonstrate angiogenesis processes because it can show microvascular permeability. Besides, DCE–MRI enables the quantitative assessment of BBB [41]. This method has some disadvantages. It has a lower temporal resolution than DSC, which may not be optimal for adequate extraction of all parameters. DCE–MRI include postprocessing and quantification of the images.

Furthermore, there is no consensus on which pharmacokinetic model is optimal for DCE–MRI [41]. A variety of tracer kinetic models have been used to describe the behavior of injected contrast agent in DCE–MRI[42]. The Tofts model is developed for tissues with insignificant blood volume and is used to describe the permeability of the tissue vasculature. For the evaluation of the highly perfused tissues like tumor, the extended Tofts model has been introduced [42]. But neither model offers the best fit when tissue has intermediate vascularity. For the good fit, the temporal resolution need to be reduced, but it does not improve the accuracy of parameters [43]. The extended Tofts model is generally used for tumor description; it allows to obtain the important permeability parameters, which are related to tumor grade, immunohistochemical markers of tumor angiogenesis, and microvessel density [44]. Using this model, the different pharmacokinetic parameters, such as V_p (fractional volume of vascular plasma space) representing angiogenesis, K^{trans} (volume transfer constant: between the plasma and extravascular extracellular space) and V_e (fractional volume of extravascular extracellular space) reflecting vascular permeability, can be estimated [45]. Meanwhile, only K^{trans} and V_e can be estimated with the Tofts model[44].

Previous studies have revealed that DCE–MRI can help predict the

prognosis after surgical resection followed by standard therapy as well as histologic grading and differentiate pseudoprogression from true progression [41,45–47]. Other study demonstrated, that K^{trans} from the non-enhancing T2 HSI lesions is a potential prognostic marker for progression in glioblastoma patients[28].However, these results have demonstrated only the group difference (i.e., between progression and non-progression) using a single statistical parameter such as median and 99th percentile K^{trans} , which suggests the possibility of developing a good prognostication model using DCE–MRI.

In parallel to the development of precision medicine, there has been growing interest on radiomics [48]. The words, which end in –omics refer to the field of biological sciences[49]. Unlike other high-dimensional omics data radiomics demonstrates unique characteristics, as there is no direct biological connection and the stability of feature largely depends on image itself[50]. Radiomics is a process of converting digital medical images into mineable high–dimensional data. The base of the process is that both functional and morphological clinical images contain quantitative and qualitative information, which may image the pathophysiology of the underlying tissue[48]. An optimal radiomics analysis consist of four steps: 1) imaging acquisition, 2) segmentation, 3)

feature extraction, and 4) statistical analysis[51]. To extract the radiomics features, it is necessary to define ROI in which they are calculated[52].

For building robust and reliable models, every step requires careful evaluation so that they can be used in clinical practice for non-invasive disease tracking, disease prognosis, and assessment of disease response to treatment[48]. Radiomics extract high-dimensional features from image metrics such as intensity distribution, spatial relationships, and textural heterogeneity, which may reflect underlying pathophysiology, including intratumoral heterogeneity better than the single parameter approach. Several radiomics prognostication models have been successfully applied to glioblastoma using MRI [51,53,54]. Radiomic features are broadly categorized into texture, shape, and voxel intensity histogram features. Different statistical methods are used to calculate the radiomics features [55]. They are subdivided into the following: 1) First-order statistic which characterizes the distribution of individual voxels without regard to spatial relationships[48], 2) Textural statistic or second-order statistic which depends on the relation between neighboring voxels[55], 3) Shape based statistic which demonstrates geometric properties and shape of the ROI[48], 4) Higher-order statistic

which is obtained by mathematical transformation of the images followed by the application of filters [48,55]. In addition, radiomic features can be extracted using transforms (wavelet transform) or filters[48]. More specifically, radiomic features have been known to have potential to reflect biological intra-tumoral heterogeneity (ITH), which is enhanced by clonal variation and tumor microenvironmental influences on tumor cells[56,57].

Recently, Park et al. have demonstrated that the prognostication model using combined radiomic features obtained from diffusion- and perfusion-weighted MRI showed improved performance over the model using only conventional MRI in glioblastoma [58].

At present, there are not many studies to analyze radiomics score obtained from DCE MRI for the prediction of a high-risk group in glioblastoma patients. The aim of our retrospective research was to develop a “radiomics risk score” based on DCE MRI for the prediction of a high-risk group in patients with glioblastoma.

Materials and methods

Patients

The institutional review board of Seoul National University Hospital (IRB No. 2006-144-1134) approved this retrospective study and the requirement for written informed consent was waived. Between January 2011 and July 2019, 274 patients with initially diagnosed glioblastoma were recruited from the radiology report database at the hospital. The followings were the inclusion criteria: the patients (a) had a histopathologic diagnosis of glioblastoma based on the 2016 World Health Organization (WHO) classification of central nervous system tumors, (b) underwent preoperative 3.0-Tesla (3T) MRI 24-48 hours before the operation, including contrast-enhanced (CE) T1-weighted imaging (T1WI), DCE-MRI and FLAIR imaging, (c) underwent the standard concomitant chemoradiotherapy[5] with temozolomide (TMZ) and 6 cycles of adjuvant TMZ after maximal surgical resection of contrast-enhancing region, (d) had follow-up period of \geq one year at least after surgery with or without disease progression, and (e) O6-methylguanine DNA methyltransferase (MGMT) methylation status was identified. We specified the extent of resection as maximal (near-total or gross-total) resection, because we aimed to focus on investigating the effect of non-

enhancing T2 hyperintense areas of glioblastoma for prognosis, excluding the recurrence from gross residual tumor [29,47]. The exclusion criteria: (a) incomplete pre-operative DCE-MRI (n=27), (b) other treatment regimen except standard treatment (n=61), or (c) patients with follow-up loss (n=36).

According to the Response Assessment in Neuro-Oncology criteria, all patients were classified into disease progression and non-progression groups at one year after the completion of adjuvant TMZ, following the previous study [45]. Patients, who have any of the followings were considered to have disease progression: (A) significant increase in non-enhancing T2-weighted FLAIR lesions, not attributable to other non-tumor causes, (B) a greater than 25% increase in the sum of the products of the perpendicular diameters of the enhancing lesions with the smallest tumor measurement, (C) any new lesions, and (D) clinical deterioration not attributable to other non-tumor causes and not due to steroid decrease. Thus, the progression of disease was confirmed either by following imaging or by histopathologic diagnosis. In case there was evident increase in enhancing lesions that did not meet the criteria of progression, short-term (i.e. 1-2 months) follow-up imaging was performed. The progression-free survival (PFS) was calculated between

the date of initial imaging of diagnosis and the date confirmed as progression. If there was no evidence of disease at the last follow-up, then the PFS was calculated between the date of initial imaging of diagnosis and the last follow-up. We referred to the electronic medical records by clinicians at our institution to distinguish progression from non-progression.

For all patients, clinical characteristics including age, sex, methylation status of MGMT tumor promoter, and isocitrate dehydrogenase (IDH) mutation status were recorded.

Imaging protocol

All MR images were acquired using a 3T scanner (Verio, Trio or Skyra; Siemens, Erlangen, Germany), using a 32-channel head coil. For tumor segmentation, the T1-weighted 3D magnetization-prepared rapid acquisition gradient echo (MPRAGE) sequence before and after administration of gadobutrol (Gadovist; Bayer, Berlin, Germany; at a dose of 0.1 mmol/kg of body weight) and FLAIR imaging were used. We performed the transverse T1WI with the following parameters: a repetition time (TR) of 558 ms, an echo time (TE) of 9.8 ms, a flip angle (FA) of 70° , a matrix of 384×187 , a field of view (FOV) of 175×220 , a

section thickness of 5 mm, and a number of excitations (NEX) of 1. The parameters for 3D MPRAGE were a TR of 1500 ms, a TE of 1.9 ms, a FA of 9° , a matrix of 256×232 , a FOV of 220×250 , a section thickness of 1 mm, and a NEX of 1. The parameters for transverse FLAIR were a TR of 9000ms, a TE of 97 ms, a TI of 2500 ms, a FA of 130° , a matrix of 384×348 , a FOV of 199×220 , a section thickness of 5 mm, and a NEX of 1. We acquired the transverse T2WI with the following parameters: a TR of 5160ms, a TE of 91ms, a FA of $124\text{--}130^\circ$, a matrix of $640 \times 510\text{--}580$, a FOV of 199×220 , a section thickness of 5 mm and a NEX of 3.

DCE-MRI was conducted with 3D gradient-echo T1WI after the intravenous administration of gadobutrol at a dose of 0.1 mmol/kg of body weight at a rate of 4 mL/s using a power injector (Spectris MedRad, Indianola, Pennsylvania). After the contrast, a 30 mL saline bolus was injected at the same injection rate. For each section, 40 images were acquired at intervals equal to the TR. The scan parameters of DCE MRI were a TR of 2.8 ms, a TE of 1.0 ms, a FA of 10° , a matrix of 192×192 , a FOV of 240×240 , a section thickness of 3 mm, a voxel size of $1.25 \times 1.25 \times 3 \text{ mm}^3$, a pixel bandwidth of 789 Hz, and a total acquisition time of 5 min 8 s.

Image processing and analysis

The MR data including CE T1WI, FLAIR imaging, and DCE–MRI were transferred from the PACS workstation to a personal computer and processed with a software package (Nordic ICE v4.1.2; NordicNeuroLab, Bergen, Norway). DCE–MRI analysis based on the two–compartment pharmacokinetic model suggested by Tofts and Kermode and pharmacokinetic parameters, including the volume transfer constant (K^{trans}), the extravascular extracellular space volume per unit volume of tissue (V_e) and the blood plasma volume per unit volume of tissue (V_p) [29] were calculated. More specifically, deconvolution with the arterial input function (AIF) was performed using the two–compartment pharmacokinetic model. AIF was selected in tumor–supplying arteries near the tumor. Each parameter was calculated by using the fixed T1 measurement of 1000 ms.

Before drawing regions of interest (ROIs), we reconstructed CE T1WI from sagittal to axial plane, acquired K^{trans} , V_e and V_p maps based on DCE MRI, and resampled the size of CE T1WI and FLAIR images using one of the map (K^{trans} , V_p and V_e) as reference. We drew two ROIs, (a) the non–enhancing T2 high signal intensity (SI) areas and (b) enhancing tumor without cystic or necrotic regions on CE T1WI. We carefully excluded the vessels in all ROIs. All ROIs were drawn semi–automatically using seed

growing and threshold segmentation and were corrected manually, if needed [59]. ROIs were drawn by a radiologist (E.P.) under the supervision of one expert radiologist (S.H.C., with 17 years of neuro-oncology imaging experience).

In our research, we used the Pyradiomics package software 3D Slicer 4.11.0 for the extraction of the radiomic features. For each patient, total 642 features were obtained: 107 features including 18 first-order, 24 gray level co-occurrence matrix (GLCM), 14 shape-based, 16 gray level run length matrix (GLRLM), 16 gray level size zone matrix (GLSZM), 14 gray level dependence matrix (GLDM), 5 neighboring gray tone difference matrix (NGTDM) features from each of K^{trans} , V_e , and V_p map, respectively. Both enhancing region and non-enhancing T2 high SI region masks were used, which makes 6 map-region combinations per patient. The details of radiomic features are described in Supplementary materials.

Radiomic feature selection

The patients were randomly split into the discovery set ($n = 105$) and the validation set ($n = 45$) in a 7:3 ratio. The radiomic feature selection using the discovery set included three steps: first, features with more than 10% outliers were discarded where outliers were defined if the largest

and smallest 10% value of features are larger than median ± 3 median absolute deviation (MAD) [60]. Standardization, or z-score normalization, was followed for each feature. Here, we used the mean and standard deviation of discovery set to standardize the validation set to prevent the data leakage, which may lead to the decrease in the generalized model performance [61,62]. Second, univariate Cox regression was performed to select significant features. Subsequently, a Cox-least absolute shrinkage selector operator (Cox-LASSO) model was developed to select the final radiomic features in the prediction of PFS using *glmnet* R package. LASSO has been a popular regularization method for selecting features from multiple variables, penalizing the coefficients of variables by shrinking some of them to zero in the regression model, leaving the other variables with non-zero coefficients [63]. To determine hyperparameter λ in LASSO, 10-fold cross-validation was performed using *cv.glmnet*.

Radiomics score and risk stratification

A radiomics score model was developed using a weighted combination of the final selected features in the discovery set. Subsequently, the cut-off value of radiomics scores obtained by maximally selected rank statistics using *maxstat* (R package) [64,65] was applied to stratify the patients

into either a low- or high-risk group in the discovery and validation sets [62]. In other words, the “radiomics risk score” was present when the radiomics score of the patient was higher than the median cut-off value.

Tissue diagnosis and genetic analysis

Immunohistochemical staining was performed using a BenchMark XT (automated immunohistochemical slide staining system, Roche Diagnostics, IN, USA). Immunohistochemistry (IHC) was performed on individual whole block sections using antibodies against IDH1 R132H mutant protein (H09, Dianova, Hamburg, Germany, 1:50). If IDH1 IHC was negative, direct Sanger sequencing of IDH1/IDH2 was performed. O6 methylguanine methyltransferase methylation-Specific PCR (MGMT-MSP) using a methylation EZ kit was used to evaluate the methylation status of the MGMT promoter.

Progression free survival analysis

A multivariate Cox-regression model was developed using clinical variables: age, sex, status of IDH mutation, and status of MGMT methylation, in addition to the risk group variable derived from radiomics score. To validate the developed radiomics score, the radiomics score was

calculated using values of selected features of validation set, weighted by the coefficients obtained from the discovery set. Using the median value of the radiomics score as the cutoff value, which was obtained from the discovery set, validation set was stratified into either a high- or low-risk group according to one-year PFS. All the statistical analysis was performed using R-3.6.3 (R-core Team, Vienna, Austria), and p -value of 0.05 was considered significant. The overall process from the feature extraction to risk group stratification is illustrated in Fig. 1.

Results

Patient characteristics

A total of 150 patients were enrolled in this study, according to inclusion/exclusion criteria (Fig. 2): 92 (61.3%) male; mean age 60.5 ± 13.5 years old; and 137 (91.3%) IDH-wildtype (Table 1). The patients were divided into the disease progression group ($n = 61$, 40.7%), and the non-progression group ($n = 89$, 59.3%) at one year after surgery. The median progression free survival was 11.1 months (range, 0.57–97.0 months). Patients with O6-Methylguanine-DNA methyltransferase (MGMT) promotor methylated status were more frequently observed in the non-progression group than in the progression group (61 of 89 vs 20 of 61, respectively, $p < 0.001$). Patient characteristics are detailed in Table 1. There were no significant clinicopathologic differences: age ($p=0.149$), sex ($p=1.000$), IDH ($p=1.000$), MGMT ($p=0.253$), and number of recurrence ($p=0.093$) between discovery and validation set (Table 2).

Selected features and a radiomics score

As a result of discarding outliers using 3 MAD, 589 from total 642 features were left. After univariate Cox-regression, 76 significant

features were left, and 16 features were selected by a Cox–LASSO model in the prediction of PFS. The intermediate results of Cox–LASSO procedure are given in Fig. 3, and for 76 selected features from univariate Cox–regression, a heatmap of radiomic features using hierarchical clustering with dendrogram is provided in Fig. 4. Intermediate results in the procedure of cox–LASSO model using training set are illustrated in Fig. 5. The 16 features selected were 7 features from K^{trans} , and the other 9 features from V_e map of non–enhancing T2 high SI region: 1 NGTDM feature, 3 GLDM features, 1 first–order feature, 5 GLRLM features, 3 shape features, 1 GLCM feature, and 2 GLSZM features (Table 3). A radiomics score model was developed using a linear combination of the 16 final selected features with coefficients obtained from Cox–LASSO model using the discovery set (Eq. 1)

Radiomics score

$$\begin{aligned}
&= \text{gldm_SmallDependenceEmphasis_NE_V}_e \times 0.186 \\
&+ \text{gldm_SmallDependenceHighGrayLevelEmphasis_NE_V}_e \\
&\quad \times 0.119 + \text{firstorder_Energy_NE_V}_e \\
&\quad \times 0.114 + \cdots + \text{glcm_JointAverage_NE_V}_e \times 0.029 \\
&+ \text{shape_MajorAxisLength_NE_V}_e \times 0.005 \\
&+ \text{gldm_GrayLevelVariance_NE_V}_e \times 0.001 \text{ (Eq.1)}
\end{aligned}$$

Patient stratification using radiomics risk score

The radiomics score was computed using the 16 selected features obtained from the discovery set for each discovery and validation set. In a univariate Cox-regression with the risk group variable based on the radiomics score, or the “radiomics risk score”, the radiomics risk score stratified high- and low-risk group in both the validation and discovery set in log-rank test (both $p < 0.001$) (Fig. 6). The cut-off value of 0.374 was obtained using maximally selected rank variables ($M = 3.277$; $p = 0.017$). The intermediate results are illustrated in Fig. 7. Representative cases are shown in Fig. 8 and 9.

Multivariate Cox-regression model adding clinical variables

A multivariate Cox-regression model was developed using clinical variables: age, sex, status of IDH mutation, and status of MGMT methylation, in addition to the “radiomics risk score” (concordance, or C-index = 0.678 ± 0.051). The presence of high radiomics risk score, and IDH mutation were significant variables: HR = 3.56, $p = 0.004$; and HR = 0.34, $p = 0.022$, respectively. In other words, IDH mutation group showed about 3 times stronger association to progression than the wildtype group; and the high radiomics risk score group showed about 3.5

times stronger association to progression than the low risk score group. A forest plot of multivariate Cox–regression model is shown in Fig. 10. For each single variable, the stratification of survival curves was plotted in Fig. 11.

Discussion

In present research, we developed and assessed the “radiomics risk score” from V_e , V_p and K^{trans} maps of DCE-MRI to show the diagnostic capability in the prediction of the high-risk group in glioblastoma. Our approaches could be useful for the followings: first, the textural features of the K^{trans} and V_e maps based on non-enhancing T2 high SI areas played a crucial role for the risk stratification in recurrence of glioblastoma ($p < 0.001$ in both the training and validation sets; log-rank test). Second, the radiomics risk score was independent of IDH mutation status in cox-regression analysis (HR = 3.56, $p = 0.004$; HR = 0.34, $p = 0.022$, respectively), providing an additional surrogate marker for progression in glioblastoma. The final selected 16 radiomic features out of 642 features were obtained from non-enhancing T2 hyperintense lesions: 9 features (*gldm_SmallDependenceEmphasis* showing the largest coefficient) from V_e map; and the other 7 features (*glrlm_ShortRunHighGrayLevelEmphasis* showing the largest coefficient) from K^{trans} map. In other words, the textural features obtained from non-enhancing T2 high SI areas of K^{trans} and V_e maps, significantly stratified the low- and high-risk groups (Eq. 1 and Table 3), which was independent of IDH mutation status, one of the most important risk factors. Thus, radiomic features can predict the

prognosis of glioblastoma, reflecting intra-tumoral heterogeneity of “permeability” of non-enhancing T2 hyperintense areas using DCE-MRI, because textural features provide a measure of the spatial arrangement of the intra-lesional voxel intensities, which are obtained by calculating the statistical inter-relationships between neighboring voxel intensities [48].

Our results demonstrate that radiomic features from non-enhancing T2 hyperintense lesions were more important than contrast-enhancing lesions to predict the progression, especially when total resection was performed, in keeping with the results of the previous studies [66,67]. Non-enhancing T2 hyperintense region on the tumor margin has been named “peritumoral edema” . Peritumoral edema is associated with of the degree of neovascularisation and the expression of vascular endothelial growth factor (VEGF). In other words, the VEGF expression and enlargement of peritumoral edema may be prognostic marker for glioblastoma patients [68]. The non-enhancing T2 hyperintense area is a mixture of infiltrating tumor cells and vasogenic edema, where fluid penetrates into the parenchymal extracellular space [67]. Schoenegger et al. showed that the extent of the edema is an independent prognostic factor glioblastoma patients [69]. However, it is not possible to

differentiate vasogenic edema from infiltrating tumor with conventional imaging sequences [67].

Recent researches have shown that perfusion characteristics obtained from perfusion-weighted MRI predict not only progression/survival, but also crucial tumor characteristics such as genetic mutations in glioblastoma [45,59,70]. Among perfusion-weighted MR techniques, DCE-MRI images the perfusion characteristics of the tumors which cannot be provided in the conventional MRI sequence, reflecting the exchange between the vasculature in tissue and interstitium, or “leakage space” [29]. Pharmacokinetic parameters are obtained from DCE-MRI which represent the tissue permeability: K^{trans} , the volume transfer constant between the plasma and the extravascular extracellular space, has the capability of predicting the histologic grading of gliomas, because higher grade gliomas show enhanced angiogenesis, resulting in immature vessels of higher permeability [29,71]; and V_e , the extravascular extracellular space volume per unit volume of tissue, is also a predictor of progression in high grade glioma patients [72]. Kim et al. showed that the analysis of DCE MR parameters of non-enhancing T2 high SI lesions could predict the progression in glioblastoma. The 99th percentile K^{trans} value of non-enhancing T2 hyperintense lesions in glioblastoma was

useful in prediction of early disease progression [29]. Moreover, the 97th percentile V_e value could also differentiate non-progression from progression using univariate analysis [29]. The results imply that infiltrative tumor cells in non-enhancing areas, residing outside the enhancing portion, could serve as surrogate markers of the prognosis and aggressiveness of glioblastoma [29]. Hwang et al. also reported that increased preoperative median K^{trans} from non-enhancing T2 high SI lesions was associated with poor survival in patients with gross total resection followed by standard therapy, using multivariate Cox regression analysis [47]. In our study, the radiomics risk score obtained from K^{trans} and V_e maps of non-enhancing T2 high SI lesions showed diagnostic capability in risk stratification of glioblastoma, which is also consistent with the previous studies.

Radiomics extracts high-dimensional features from image metrics such as intensity distribution, spatial relationships, and textural heterogeneity, which may reflect underlying pathophysiology including intratumoral heterogeneity, and several radiomics prognostication models for glioblastoma have been developed and validated using radiomic features obtained from MRI [51,53,54]. However, high-dimensionality ($d = 642$) of radiomics data, or much higher dimension of data compared to the

number of the subjects in the discovery set ($n = 105$), causes the “curse of dimensionality” , leading to “overfitting” of the model to the discovery set. In other words, the model developed using radiomics data may show good performance only in discovery set, but not in validation set, or show low “generalizability” [73]. Here, to overcome this issue, we used Cox–LASSO model to select the significant radiomic features in the prediction of PFS. LASSO has been a popular regularization method for selecting features from multiple variables, because it penalizes and imposes the coefficients of some variables to shrink toward zero in the regression model. This leaves the other variables with non–zero coefficients, selecting important features [63], which in turn alleviates the “curse of dimensionality” due to high dimensionality in radiomics data analysis [74].

Isocitrate dehydrogenase (IDH) is an enzyme that catalyze the oxidative decarboxylation of isocitrate to α –ketoglutarate [75]. IDH1/2 mutation has been known to one of the most important molecular biomarker of glioblastoma with diagnostic, prognostic, and predictive role: IDH–mutant group demonstrates better survival as compared with IDH–wildtype [76]; IDH mutation is a significant marker of the positive chemo sensitivity of secondary glioblastoma [77]; and maximal surgical resection of the IDH–

mutant group provides a survival benefit [78]. Reflecting these results, glioblastomas are categorized in the 2016 CNS WHO classification into (1) primary glioblastomas, IDH-wildtype (about 90% of cases), (2) secondary glioblastomas, IDH-mutant (about 10% of cases). Secondary glioblastomas show signs of progression from a lower-grade tumor, while primary glioblastomas present as advanced cancers at diagnosis [79]. The IDH1/2 mutations make the tumor microenvironment easier to form and increase invasiveness [80]. Previous researches have demonstrated that the radiomics model built with multiregional features from multiparametric MRI has the potential to preoperatively detect the IDH1 mutation status in glioblastoma patients [81,82]. Tan et al showed that IDH, age and radiomics signature are independent risk factors in high-grade glioma [83]. Here, our study showed that the developed radiomics risk score increased the risk of progression in glioblastoma patients, independently of IDH-mutation status (HR = 3.56, $p = 0.004$; HR = 0.34, $p = 0.022$, respectively).

Our study has several limitations. First, the study was retrospective, and the number of patients was limited for sufficient extraction of significant radiomic features, which warrants further improvement of the radiomics risk score with a larger number of patients. Second, time-

consuming, multi-staged workflow including manual ROI drawing discourages the application of the developed radiomics risk score in clinical practice. The automated segmentation technique could relieve the problem effectively. Third, radiomic features are sensitive to imaging parameters and systems, which may make the radiomics models fail in multi-centered and prospective applications. “Harmonization” of multi-centered radiomics could improve the generalizability, which is our next research topic. Fourth, although there was no significant clinicopathologic difference between validation and discovery sets in the present research, the discovery and validation sets were randomly split, instead of using a stratified split, which might improve the model performance.

In conclusion, we developed and assessed the radiomics risk score obtained from DCE-MRI for the risk stratification of progression in glioblastoma. The radiomics risk score, mainly extracted from non-enhancing T2 hyperintense areas rather than contrast-enhancing areas, a high-risk patient independently of IDH mutation, providing an additional surrogate marker of disease progression.

References

- [1] F. Hanif, K. Muzaffar, K. Perveen, S.M. Malhi, S.U. Simjee, Glioblastoma Multiforme: A Review of its Epidemiology and Pathogenesis through Clinical Presentation and Treatment, *Asian Pac J Cancer Prev* 18 (2017) 3–9. [10.22034/APJCP.2017.18.1.3](https://doi.org/10.22034/APJCP.2017.18.1.3).
- [2] J.F. de Groot, High-grade gliomas, *Continuum (Minneapolis, Minn)* 21 (2015) 332–344. [10.1212/01.CON.0000464173.58262.d9](https://doi.org/10.1212/01.CON.0000464173.58262.d9).
- [3] S. Banerjee, S. Mitra, F. Masulli, S. Rovetta, Glioma Classification Using Deep Radiomics, *SN Computer Science* 1 (2020) 209. [10.1007/s42979-020-00214-y](https://doi.org/10.1007/s42979-020-00214-y).
- [4] M.E. Davis, Glioblastoma: Overview of Disease and Treatment, *Clin J Oncol Nurs* 20 (2016) S2–S8. [10.1188/16.CJON.S1.2-8](https://doi.org/10.1188/16.CJON.S1.2-8).
- [5] R. Stupp, W.P. Mason, M.J. van den Bent, M. Weller, B. Fisher, M.J.B. Taphoorn, K. Belanger, A.A. Brandes, C. Marosi, U. Bogdahn, J. Curschmann, R.C. Janzer, S.K. Ludwin, T. Gorlia, A. Allgeier, D. Lacombe, J.G. Cairncross, E. Eisenhauer, R.O. Mirimanoff, Radiotherapy plus Concomitant and Adjuvant Temozolomide for Glioblastoma, *The New England Journal of Medicine* 352 (2005) 987–996. [10.1056/NEJMoa043330](https://doi.org/10.1056/NEJMoa043330).

- [6] Q.T. Ostrom, G. Cioffi, H. Gittleman, N. Patil, K. Waite, C. Kruchko, J.S. Barnholtz–Sloan, CBTRUS Statistical Report: Primary Brain and Other Central Nervous System Tumors Diagnosed in the United States in 2012–2016, *Neuro Oncol* 21 (2019) v1–v100. [10.1093/neuonc/noz150](https://doi.org/10.1093/neuonc/noz150).
- [7] R. Quan, H. Zhang, Z. Li, X. Li, Survival analysis of patients with glioblastoma treated by long–term administration of temozolomide, *Medicine* 99 (2020).
- [8] B.N. Nandeesh, S. Naskar, A.H. Shashtri, A. Arivazhagan, V. Santosh, Recurrent Glioblastomas Exhibit Higher Expression of Biomarkers with Stem–like Properties, *J Neurosci Rural Pract* 9 (2018) 86–91. [10.4103/jnrp.jnrp_417_17](https://doi.org/10.4103/jnrp.jnrp_417_17).
- [9] X. Chen, Y. Yan, J. Zhou, L. Huo, L. Qian, S. Zeng, Z. Li, J. Wei, Z. Xu, Z. Gong, Clinical prognostic value of isocitrate dehydrogenase mutation, O–6–methylguanine–DNA methyltransferase promoter methylation, and 1p19q co–deletion in glioma patients, *Ann Transl Med* 7 (2019) 541–541. [10.21037/atm.2019.09.126](https://doi.org/10.21037/atm.2019.09.126).
- [10] M. Karsy, J.A. Neil, J. Guan, M.A. Mahan, H. Colman, R.L. Jensen, A practical review of prognostic correlations of molecular biomarkers in glioblastoma, *Neurosurg Focus* 38 (2015) E4. [10.3171/2015.1.Focus14755](https://doi.org/10.3171/2015.1.Focus14755).

- [11] L. Egaña, J. Auzmendi-Iriarte, J. Andermatten, J. Villanua, I. Ruiz, A. Elua-Pinin, P. Aldaz, A. Querejeta, C. Sarasqueta, F. Zubia, A. Matheu, N. Samprón, Methylation of MGMT promoter does not predict response to temozolomide in patients with glioblastoma in Donostia Hospital, *Scientific Reports* 10 (2020) 18445. [10.1038/s41598-020-75477-9](https://doi.org/10.1038/s41598-020-75477-9).
- [12] A.L. Cohen, H. Colman, *Glioma Biology and Molecular Markers*, in: J. Raizer, A. Parsa (Eds.) *Current Understanding and Treatment of Gliomas*, Springer International Publishing, Cham, 2015, pp. 15–30.
- [13] D. Krex, B. Klink, C. Hartmann, A. von Deimling, T. Pietsch, M. Simon, M. Sabel, J.P. Steinbach, O. Heese, G. Reifenberger, M. Weller, G. Schackert, N. for the German Glioma, Long-term survival with glioblastoma multiforme, *Brain* 130 (2007) 2596–2606. [10.1093/brain/awm204](https://doi.org/10.1093/brain/awm204).
- [14] R. Stupp, M.E. Hegi, W.P. Mason, M.J. van den Bent, M.J.B. Taphoorn, R.C. Janzer, S.K. Ludwin, A. Allgeier, B. Fisher, K. Belanger, P. Hau, A.A. Brandes, J. Gijtenbeek, C. Marosi, C.J. Vecht, K. Mokhtari, P. Wesseling, S. Villa, E. Eisenhauer, T. Gorlia, M. Weller, D. Lacombe, J.G. Cairncross, R.-O. Mirimanoff, Effects of radiotherapy with concomitant and adjuvant temozolomide versus radiotherapy alone on survival in glioblastoma in a randomised phase III study: 5-year analysis of the EORTC-NCIC trial,

The Lancet Oncology 10 (2009) 459–466.

[https://doi.org/10.1016/S1470-2045\(09\)70025-7](https://doi.org/10.1016/S1470-2045(09)70025-7).

[15] L. Treps, S. Edmond, E. Harford–Wright, E.M. Galan–Moya, A. Schmitt, S. Azzi, A. Citerne, N. Bidère, D. Ricard, J. Gavard, Extracellular vesicle–transported Semaphorin3A promotes vascular permeability in glioblastoma, *Oncogene* 35 (2016). 10.1038/onc.2015.317.

[16] S.W. Schneider, T. Ludwig, L. Tatenhorst, S. Braune, H. Oberleithner, V. Senner, W. Paulus, Glioblastoma cells release factors that disrupt blood–brain barrier features, *Acta Neuropathologica* 107 (2004) 272–276. 10.1007/s00401-003-0810-2.

[17] P. Ballabh, A. Braun, M. Nedergaard, The blood–brain barrier: an overview: Structure, regulation, and clinical implications, *Neurobiology of Disease* 16 (2004) 1–13. <https://doi.org/10.1016/j.nbd.2003.12.016>.

[18] L.G. Dubois, L. Campanati, C. Righy, I. D’ Andrea–Meira, T.C.L.d.S.e. Spohr, I. Porto–Carreiro, C.M. Pereira, J. Balça–Silva, S.A. Kahn, M.F. DosSantos, M.d.A.R. Oliveira, A. Ximenes–da–Silva, M.C. Lopes, E. Faveret, E.L. Gasparetto, V. Moura–Neto, Gliomas and the vascular fragility of the blood brain barrier, *Frontiers in Cellular Neuroscience* 8 (2014). 10.3389/fncel.2014.00418.

[19] Y. Kang, E.K. Hong, J.H. Rhim, R.E. Yoo, K.M. Kang, T.J. Yun, J.H.

Kim, C.H. Sohn, S.W. Park, S.H. Choi, Prognostic Value of Dynamic Contrast-Enhanced MRI-Derived Pharmacokinetic Variables in Glioblastoma Patients: Analysis of Contrast-Enhancing Lesions and Non-Enhancing T2 High-Signal Intensity Lesions, *Korean J Radiol* 21 (2020) 707-716. 10.3348/kjr.2019.0629.

[20] S.D. McGarry, S.L. Hurrell, A.L. Kaczmarowski, E.J. Cochran, J. Connelly, S.D. Rand, K.M. Schmainda, P.S. LaViolette, Magnetic Resonance Imaging-Based Radiomic Profiles Predict Patient Prognosis in Newly Diagnosed Glioblastoma Before Therapy, *Tomography* 2 (2016) 223-228. 10.18383/j.tom.2016.00250.

[21] C.-X. Wu, G.-S. Lin, Z.-X. Lin, J.-D. Zhang, S.-Y. Liu, C.-F. Zhou, Peritumoral edema shown by MRI predicts poor clinical outcome in glioblastoma, *World Journal of Surgical Oncology* 13 (2015) 97. 10.1186/s12957-015-0496-7.

[22] L. Tselikas, R. Souillard-Scemama, O. Naggara, C. Mellerio, P. Varlet, E. Dezamis, J. Domont, F. Dhermain, B. Devaux, F. Chrétien, J.-F. Meder, J. Pallud, C. Oppenheim, Imaging of gliomas at 1.5 and 3 Tesla - A comparative study, *Neuro-oncology* 17 (2015) 895-900. 10.1093/neuonc/nou332.

[23] C. Krautmacher, W.A. Willinek, H.J. Tschampa, M. Born, F. Träber,

J. Gieseke, H.J. Textor, H.H. Schild, C.K. Kuhl, Brain Tumors: Full- and Half-Dose Contrast-enhanced MR Imaging at 3.0 T Compared with 1.5 T—Initial Experience, *Radiology* 237 (2005) 1014–1019. 10.1148/radiol.2373041672.

[24] M.H. Pui, E.C. Fok, MR imaging of the brain: comparison of gradient-echo and spin-echo pulse sequences, *American Journal of Roentgenology* 165 (1995) 959–962. 10.2214/ajr.165.4.7677001.

[25] M. Markl, J. Leupold, Gradient echo imaging, *Journal of Magnetic Resonance Imaging* 35 (2012) 1274–1289. <https://doi.org/10.1002/jmri.23638>.

[26] L.J. Bagley, R.I. Grossman, K.D. Judy, M. Curtis, L.A. Loevner, M. Polansky, J. Detre, Gliomas: correlation of magnetic susceptibility artifact with histologic grade, *Radiology* 202 (1997) 511–516. 10.1148/radiology.202.2.9015082.

[27] H.H. Park, T.H. Roh, S.G. Kang, E.H. Kim, C.-K. Hong, S.H. Kim, S.S. Ahn, S.K. Lee, H.J. Choi, J. Cho, S.H. Kim, K.-S. Lee, C.-O. Suh, J.H. Chang, Pseudoprogression in glioblastoma patients: the impact of extent of resection, *Journal of Neuro-Oncology* 126 (2016) 559–566. 10.1007/s11060-015-2001-0.

[28] S.W. Jo, S.H. Choi, E.J. Lee, R.E. Yoo, K.M. Kang, T.J. Yun, J.H. Kim,

C.H. Sohn, Prognostic Prediction Based on Dynamic Contrast-Enhanced MRI and Dynamic Susceptibility Contrast-Enhanced MRI Parameters from Non-Enhancing, T2-High-Signal-Intensity Lesions in Patients with Glioblastoma, *Korean J Radiol* (2021). 10.3348/kjr.2020.1272.

[29] R. Kim, S.H. Choi, T.J. Yun, S.T. Lee, C.K. Park, T.M. Kim, J.H. Kim, S.W. Park, C.H. Sohn, S.H. Park, I.H. Kim, Prognosis prediction of non-enhancing T2 high signal intensity lesions in glioblastoma patients after standard treatment: application of dynamic contrast-enhanced MR imaging, *Eur Radiol* 27 (2017) 1176-1185. 10.1007/s00330-016-4464-6.

[30] Y. Chen, S.J. Almarzouqi, M.L. Morgan, A.G. Lee, T1-Weighted Image, in: U. Schmidt-Erfurth, T. Kohnen (Eds.) *Encyclopedia of Ophthalmology*, Springer Berlin Heidelberg, Berlin, Heidelberg, 2018, pp. 1747-1750.

[31] A. Zimny, L. Zińska, J. Bładowska, M. Neska-Matuszewska, M. Sęsiadek, Intracranial lesions with high signal intensity on T1-weighted MR images - review of pathologies, *Pol J Radiol* 78 (2013) 36-46. 10.12659/PJR.889663.

[32] V. Sawlani, M.D. Patel, N. Davies, R. Flintham, R. Wesolowski, I. Ughratdar, U. Pohl, S. Nagaraju, V. Petrik, A. Kay, S. Jacob, P. Sanghera,

V. Wykes, C. Watts, H. Poptani, Multiparametric MRI: practical approach and pictorial review of a useful tool in the evaluation of brain tumours and tumour-like lesions, *Insights into Imaging* 11 (2020) 84. 10.1186/s13244-020-00888-1.

[33] L. Zhang, L.-q. Yang, L. Wen, S.-q. Lv, J.-h. Hu, Q.-r. Li, J.-p. Xu, R.-f. Xu, D. Zhang, Noninvasively Evaluating the Grading of Glioma by Multiparametric Magnetic Resonance Imaging, *Academic Radiology* 28 (2021) e137-e146. <https://doi.org/10.1016/j.acra.2020.03.035>.

[34] G.H. Jahng, K.L. Li, L. Ostergaard, F. Calamante, Perfusion magnetic resonance imaging: a comprehensive update on principles and techniques, *Korean J Radiol* 15 (2014) 554-577. 10.3348/kjr.2014.15.5.554.

[35] S. Aydin, E. Fatihoğlu, P.N. Koşar, E. Ergün, Perfusion and permeability MRI in glioma grading, *Egyptian Journal of Radiology and Nuclear Medicine* 51 (2020) 2. 10.1186/s43055-019-0127-3.

[36] O. Macíček, R. Jirik, J. Mikulka, M. Bartoš, A. Sprláková, M. Keřkovský, Z. Starčuk jr, K. Bartusek, T. Taxt, Time-Efficient Perfusion Imaging Using DCE- and DSC-MRI, *Measurement Science Review* 18 (2018) 262-271. 10.1515/msr-2018-0036.

[37] T. Chikui, M. Obara, A.W. Simonetti, M. Ohga, S. Koga, S. Kawano, Y. Matsuo, T. Kamintani, T. Shiraishi, E. Kitamoto, K. Nakamura, K.

Yoshiura, The Principal of Dynamic Contrast Enhanced MRI, the Method of Pharmacokinetic Analysis, and Its Application in the Head and Neck Region, International Journal of Dentistry 2012 (2012) 480659. 10.1155/2012/480659.

[38] P. Manning, S. Daghighi, M.K. Rajaratnam, S. Parthiban, N. Bahrami, A.M. Dale, D. Bolar, D.E. Piccioni, C.R. McDonald, N. Farid, Differentiation of progressive disease from pseudoprogession using 3D PCASL and DSC perfusion MRI in patients with glioblastoma, J Neurooncol 147 (2020) 681–690. 10.1007/s11060-020-03475-y.

[39] T. Yankeelov, J. Gore, Dynamic Contrast Enhanced Magnetic Resonance Imaging in Oncology: Theory, Data Acquisition, Analysis, and Examples, Current Medical Imaging Reviews 3 (2007) 91–107. 10.2174/157340507780619179.

[40] J. Zhang, H. Liu, H. Tong, S. Wang, Y. Yang, G. Liu, W. Zhang, Clinical Applications of Contrast-Enhanced Perfusion MRI Techniques in Gliomas: Recent Advances and Current Challenges, Contrast Media Mol Imaging 2017 (2017) 7064120–7064120. 10.1155/2017/7064120.

[41] B.R. van Dijken, P.J. van Laar, M. Smits, J.W. Dankbaar, R.H. Enting, A. van der Hoorn, Perfusion MRI in treatment evaluation of glioblastomas: Clinical relevance of current and future techniques, Journal of Magnetic

Resonance Imaging 49 (2019) 11–22.

[42] C. Duan, J.F. Kallehauge, G.L. Bretthorst, K. Tanderup, J.J.H. Ackerman, J.R. Garbow, Are complex DCE–MRI models supported by clinical data?, *Magn Reson Med* 77 (2017) 1329–1339. 10.1002/mrm.26189.

[43] S.P. Sourbron, D.L. Buckley, On the scope and interpretation of the Tofts models for DCE–MRI, *Magn Reson Med* 66 (2011) 735–745. <https://doi.org/10.1002/mrm.22861>.

[44] M. Bergamino, L. Barletta, L. Castellan, G. Mancardi, L. Roccatagliata, Dynamic Contrast–Enhanced MRI in the Study of Brain Tumors. Comparison Between the Extended Tofts–Kety Model and a Phenomenological Universalities (PUN) Algorithm, *The Journal of the Society for Computer Applications in Radiology* 28 (2015) 748–754. 10.1007/s10278–015–9788–2.

[45] R.–E. Yoo, S. Choi, T. Kim, C.–K. Park, S.–H. Park, J.–K. Won, I. Kim, S. Lee, H. Choi, S.–H. You, K. Kang, T. Yun, J.–H. Kim, C.–H. Sohn, Dynamic contrast–enhanced MR imaging in predicting progression of enhancing lesions persisting after standard treatment in glioblastoma patients: a prospective study, *European Radiology* 27 (2017) 3156–3166. 10.1007/s00330–016–4692–9.

- [46] A.A. Thomas, J. Arevalo–Perez, T. Kaley, J. Lyo, K.K. Peck, W. Shi, Z. Zhang, R.J. Young, Dynamic contrast enhanced T1 MRI perfusion differentiates pseudoprogression from recurrent glioblastoma, *Journal of neuro–oncology* 125 (2015) 183–190.
- [47] I. Hwang, S.H. Choi, C.–K. Park, T. Kim, S.–H. Park, J. Won, I. Kim, S.–T. Lee, R.–E. Yoo, K. Kang, Dynamic Contrast–Enhanced MR Imaging of Nonenhancing T2 High–Signal–Intensity Lesions in Baseline and Posttreatment Glioblastoma: Temporal Change and Prognostic Value, *American Journal of Neuroradiology* 41 (2020) 49–56.
- [48] R. Stefania, B. Francesca, R. Sara, O. Daniela, F. Cristiana, M. Alessio Giuseppe, B. Massimo, Radiomics: the facts and the challenges of image analysis, *European Radiology Experimental* 2 (2018) 1–8. 10.1186/s41747–018–0068–z.
- [49] M. Vailati Riboni, V. Palombo, J. Loor, *What Are Omics Sciences?*, 2017, pp. 1–7.
- [50] J.E. Park, S.Y. Park, H.J. Kim, H.S. Kim, Reproducibility and Generalizability in Radiomics Modeling: Possible Strategies in Radiologic and Statistical Perspectives, *Korean J Radiol* 20 (2019) 1124–1137.
- [51] H.J. Aerts, E.R. Velazquez, R.T. Leijenaar, C. Parmar, P. Grossmann, S. Carvalho, J. Bussink, R. Monshouwer, B. Haibe–Kains, D. Rietveld,

Decoding tumour phenotype by noninvasive imaging using a quantitative radiomics approach, *Nature communications* 5 (2014) 1–9.

[52] J.E. van Timmeren, D. Cester, S. Tanadini–Lang, H. Alkadhi, B. Baessler, Radiomics in medical imaging—“how–to” guide and critical reflection, *Insights into Imaging* 11 (2020) 91. 10.1186/s13244–020–00887–2.

[53] P. Kickingereder, S. Burth, A. Wick, M. Götz, O. Eidel, H.–P. Schlemmer, K.H. Maier–Hein, W. Wick, M. Bendszus, A. Radbruch, Radiomic profiling of glioblastoma: identifying an imaging predictor of patient survival with improved performance over established clinical and radiologic risk models, *Radiology* 280 (2016) 880–889.

[54] M. Zhao, L.–L. Guo, N. Huang, Q. Wu, L. Zhou, H. Zhao, J. Zhang, K. Fu, Quantitative analysis of permeability for glioma grading using dynamic contrast–enhanced magnetic resonance imaging, *Oncol Lett* 14 (2017) 5418–5426. 10.3892/ol.2017.6895.

[55] A. Ibrahim, S. Primakov, M. Beuque, H.C. Woodruff, I. Halilaj, G. Wu, T. Refaee, R. Granzier, Y. Widaatalla, R. Hustinx, F.M. Mottaghy, P. Lambin, Radiomics for precision medicine: Current challenges, future prospects, and the proposal of a new framework, *Methods* 188 (2021) 20–29. <https://doi.org/10.1016/j.ymeth.2020.05.022>.

- [56] J.P. O'Connor, C.J. Rose, J.C. Waterton, R.A. Carano, G.J. Parker, A. Jackson, Imaging intratumor heterogeneity: role in therapy response, resistance, and clinical outcome, *Clinical Cancer Research* 21 (2015) 249–257.
- [57] P.R. Prasetyanti, J.P. Medema, Intra-tumor heterogeneity from a cancer stem cell perspective, *Molecular cancer* 16 (2017) 1–9.
- [58] J.E. Park, H.S. Kim, Y. Jo, R.-E. Yoo, S.H. Choi, S.J. Nam, J.H. Kim, Radiomics prognostication model in glioblastoma using diffusion- and perfusion-weighted MRI, *Scientific reports* 10 (2020) 1–9.
- [59] J.Y. Kim, M.J. Yoon, J.E. Park, E.J. Choi, J. Lee, H.S. Kim, Radiomics in peritumoral non-enhancing regions: fractional anisotropy and cerebral blood volume improve prediction of local progression and overall survival in patients with glioblastoma, *Neuroradiology* 61 (2019) 1261–1272. [10.1007/s00234-019-02255-4](https://doi.org/10.1007/s00234-019-02255-4).
- [60] C. Leys, C. Ley, O. Klein, P. Bernard, L. Licata, Detecting outliers: Do not use standard deviation around the mean, use absolute deviation around the median, *Journal of Experimental Social Psychology* 49 (2013) 764–766.
- [61] F. Chollet, *Deep learning with Python*, Manning New York 2018.
- [62] S. Kim, J. Shin, D.-Y. Kim, G.H. Choi, M.-J. Kim, J.-Y. Choi,

Radiomics on gadoxetic acid-enhanced magnetic resonance imaging for prediction of postoperative early and late recurrence of single hepatocellular carcinoma, *Clinical Cancer Research* 25 (2019) 3847–3855.

[63] N. Simon, J. Friedman, T. Hastie, R. Tibshirani, Regularization paths for Cox' s proportional hazards model via coordinate descent, *Journal of statistical software* 39 (2011) 1.

[64] C. Liang, Y. Huang, L. He, X. Chen, Z. Ma, D. Dong, J. Tian, C. Liang, Z. Liu, The development and validation of a CT-based radiomics signature for the preoperative discrimination of stage I–II and stage III–IV colorectal cancer, *Oncotarget* 7 (2016) 31401.

[65] N. Beig, K. Bera, P. Prasanna, J. Antunes, R. Correa, S. Singh, A.S. Bamashmos, M. Ismail, N. Braman, R. Verma, Radiogenomic-Based survival risk stratification of tumor habitat on Gd-T1w MRI is associated with biological processes in glioblastoma, *Clinical Cancer Research* 26 (2020) 1866–1876.

[66] R. Kim, S.H. Choi, T.J. Yun, S.–T. Lee, C.–K. Park, T.M. Kim, J.–H. Kim, S.–W. Park, C.–H. Sohn, S.–H. Park, I.H. Kim, Prognosis prediction of non-enhancing T2 high signal intensity lesions in glioblastoma patients after standard treatment: application of dynamic contrast-enhanced MR

imaging, *European Radiology* 27 (2017) 1176–1185. 10.1007/s00330-016-4464-6.

[67] S. Rathore, H. Akbari, J. Doshi, G. Shukla, M. Rozycki, M. Bilello, R. Lustig, C. Davatzikos, Radiomic signature of infiltration in peritumoral edema predicts subsequent recurrence in glioblastoma: implications for personalized radiotherapy planning, *J Med Imaging (Bellingham)* 5 (2018) 021219–021219. 10.1117/1.JMI.5.2.021219.

[68] C. Seidel, N. Dörner, M. Osswald, A. Wick, M. Platten, M. Bendszus, W. Wick, Does age matter? – A MRI study on peritumoral edema in newly diagnosed primary glioblastoma, *BMC Cancer* 11 (2011) 127. 10.1186/1471-2407-11-127.

[69] K. Schoenegger, S. Oberndorfer, B. Wuschitz, W. Struhal, J. Hainfellner, D. Prayer, H. Heinzl, H. Lahrmann, C. Marosi, W. Grisold, Peritumoral edema on MRI at initial diagnosis: an independent prognostic factor for glioblastoma?, *Eur J Neurol* 16 (2009) 874–878. 10.1111/j.1468-1331.2009.02613.x.

[70] K.S. Choi, S.H. Choi, B. Jeong, Prediction of IDH genotype in gliomas with dynamic susceptibility contrast perfusion MR imaging using an explainable recurrent neural network, *Neuro-Oncology* 21 (2019) 1197–1209. 10.1093/neuonc/noz095.

- [71] S.C. Jung, J. Yeom, J.-H. Kim, I. Ryoo, S. Kim, H. Shin, A. Lee, T. Yun, C.-K. Park, C.-H. Sohn, Glioma: application of histogram analysis of pharmacokinetic parameters from T1-weighted dynamic contrast-enhanced MR imaging to tumor grading, *American Journal of Neuroradiology* 35 (2014) 1103–1110.
- [72] A. Ulyte, V.K. Katsaros, E. Liouta, G. Stranjalis, C. Boskos, N. Papanikolaou, J. Usinskiene, S. Bisdas, Prognostic value of preoperative dynamic contrast-enhanced MRI perfusion parameters for high-grade glioma patients, *Neuroradiology* 58 (2016) 1197–1208. 10.1007/s00234-016-1741-7.
- [73] G.V. Trunk, A problem of dimensionality: A simple example, *IEEE Transactions on pattern analysis and machine intelligence* (1979) 306–307.
- [74] M. Verleysen, D. François, The curse of dimensionality in data mining and time series prediction, *International work-conference on artificial neural networks*, Springer, 2005, pp. 758–770.
- [75] P. Yang, W. Zhang, Y. Wang, X. Peng, B. Chen, X. Qiu, G. Li, S. Li, C. Wu, K. Yao, W. Li, W. Yan, J. Li, Y. You, C.C. Chen, T. Jiang, IDH mutation and MGMT promoter methylation in glioblastoma: results of a prospective registry, *Oncotarget* 6 (2015) 40896–40906. 10.18632/oncotarget.5683.

- [76] R. Stupp, M. Brada, M. Van Den Bent, J.-C. Tonn, G. Pentheroudakis, High-grade glioma: ESMO Clinical Practice Guidelines for diagnosis, treatment and follow-up, *Annals of oncology* 25 (2014) iii93–iii101.
- [77] Q. SongTao, Y. Lei, G. Si, Y.-q. Ding, H. HuiXia, Z. XueLin, W. LanXiao, Y. Fei, IDH mutations predict longer survival and response to temozolomide in secondary glioblastoma, *Cancer science* 103 (2012) 269–273. 10.1111/j.1349–7006.2011.02134.x.
- [78] J. Beiko, D. Suki, K.R. Hess, B.D. Fox, V. Cheung, M. Cabral, N. Shonka, M.R. Gilbert, R. Sawaya, S.S. Prabhu, IDH1 mutant malignant astrocytomas are more amenable to surgical resection and have a survival benefit associated with maximal surgical resection, *Neuro-oncology* 16 (2014) 81–91.
- [79] A.L. Cohen, S.L. Holmen, H. Colman, IDH1 and IDH2 mutations in gliomas, *Curr Neurol Neurosci Rep* 13 (2013) 345. 10.1007/s11910–013–0345–4.
- [80] J. Huang, J. Yu, L. Tu, N. Huang, H. Li, Y. Luo, Isocitrate Dehydrogenase Mutations in Glioma: From Basic Discovery to Therapeutics Development, *Front Oncol* 9 (2019) 506–506. 10.3389/fonc.2019.00506.
- [81] Z.-C. Li, H. Bai, Q. Sun, Y. Zhao, Y. Lv, J. Zhou, C. Liang, Y. Chen,

D. Liang, H. Zheng, Multiregional radiomics profiling from multiparametric MRI: Identifying an imaging predictor of IDH1 mutation status in glioblastoma, *Cancer Med* 7 (2018) 5999–6009. 10.1002/cam4.1863.

[82] K.L.-C. Hsieh, C.-Y. Chen, C.-M. Lo, Radiomic model for predicting mutations in the isocitrate dehydrogenase gene in glioblastomas, *Oncotarget* 8 (2017) 45888–45897. 10.18632/oncotarget.17585.

[83] Y. Tan, W. Mu, X.-c. Wang, G.-q. Yang, R.J. Gillies, H. Zhang, Improving survival prediction of high-grade glioma via machine learning techniques based on MRI radiomic, genetic and clinical risk factors, *European Journal of Radiology* 120 (2019) 108609. <https://doi.org/10.1016/j.ejrad.2019.07.010>.

Tables

Table 1. Clinicopathologic characteristics of the study population

Characteristics	Total (n = 150)	Progression at 1 year (n = 61)	Non–progression at 1 year (n = 89)	P value
Mean age (years)	60.5 ± 13.5	61.5 ± 13.03	59.8 ± 13.9	0.444*
The mean radiation dose (Gy)	55.2 ± 9.2	53.0 ± 11.7	56.7 ± 7.3	0.032*
Sex				0.237 [†]
male	92	41	51	
female	58	20	38	
Methylated MGMT promoter				<0.001 [†]
Positive	81 (54%)	20 (13.3%)	61 (40.7%)	
Negative	69 (46%)	41 (27.3%)	28 (18.7%)	
IDH1/2 mutation				0.075 [†]
Positive	13 (8.7%)	2 (1.3%)	11 (7.3%)	
Negative	137 (91.3%)	59 (39.3%)	78 (52%)	

Abbreviations: MGMT, O6–Methylguanine–DNA methyltransferase; IDH, isocitrate dehydrogenase.

Note: Unless otherwise specified, data are given as the number of patients.

Data are expressed as mean \pm standard deviation.

* Calculated using an unpaired Student' s t test.

† Calculated using Chi-squared/Fisher' s exact test.

Table 2. Clinicopathologic characteristics of discovery and validation set

Characteristics	Total (n = 150)	Discovery (n = 105)	Validation (n = 45)	P value
Mean age (years)	60.5 ± 13.5	61.5 ± 13.8	58.1 ± 12.8	0.149*
Sex				1.000
male	92	64	28	†
female	58	41	17	
Recurrence	81	49	32	0.093
				†
Methylated MGMT promoter				0.253
Positive	81	53	28	†
Negative	69	52	17	
IDH1/2				1.000

mutation				†
Positive	13	9	4	
Negative	137	96	41	

Abbreviations: MGMT, O6-Methylguanine-DNA methyltransferase; IDH, isocitrate dehydrogenase.

Note: Unless otherwise specified, data are given as the number of patients.

Data are expressed as mean \pm standard deviation.

* Calculated using an unpaired Student's t test.

† Calculated using Chi-squared/Fisher's exact test.

Table 3. Radiomic features selected for radiomics score

No.	Radiomic Features*	Coefficient ts ^{††}
1	gldm_SmallDependenceEmphasis_NE_Ve	0.186
2	gldm_SmallDependenceHighGrayLevelEmphasis_NE_Ve	0.119
3	firstorder_Energy_NE_Ve	0.114
4	ngtdm_Complexity_NE_Ve	0.105
5	glrlm_ShortRunHighGrayLevelEmphasis_NE_ktrans	0.100
6	glrlm_ShortRunLowGrayLevelEmphasis_NE_ktrans	0.096
7	glszm_SmallAreaEmphasis_NE_ktrans	0.091
8	shape_SurfaceArea_NE_ktrans	0.086
9	glrlm_ShortRunEmphasis_NE_ktrans	0.082
10	glszmSmallAreaHighGrayLevelEmphasis_NE_ktrans	0.071

11	glrlm_RunLengthNonUniformity_NE _ktrans	0.053
12	glrlm_ShortRunHighGrayLevelEmph asis_NE_Ve	0.044
13	shape_Maximum3DDiameter_NE_Ve	0.043
14	glcm_JointAverage_NE_Ve	0.029
15	shape_MajorAxisLength_NE_Ve	0.005
16	gldm_GrayLevelVariance_NE_Ve	0.001

Abbreviations: gldm, gray level dependence matrix features; firstorder, first-order features; ngtdm, neighbouring gray tone difference matrix features; glrlm, gray level run length matrix; glszm, gray level size zone matrix features; shape, shape-based features; glcm, gray level co-occurrence matrix features; K^{trans} , volume transfer constant; V_e , volume of the extravascular extracellular space; NE, subregion of nonenhancing T2 hyperintense lesion

† Features are listed in the descending order of coefficients.

†† coefficients are given to the third decimal place

* Each part of the feature label indicates the class, the name of features, subregion of tumor, and the pharmacokinetic parametric maps from which the features were derived, in order.

Figures

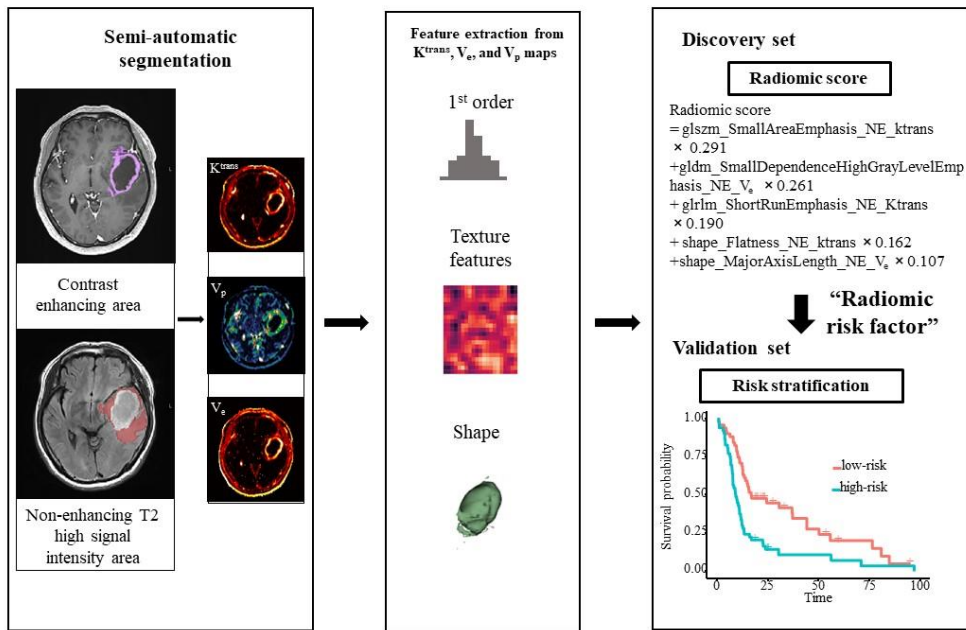


Figure 1. Overall process of radiomics score model construction and risk stratification.

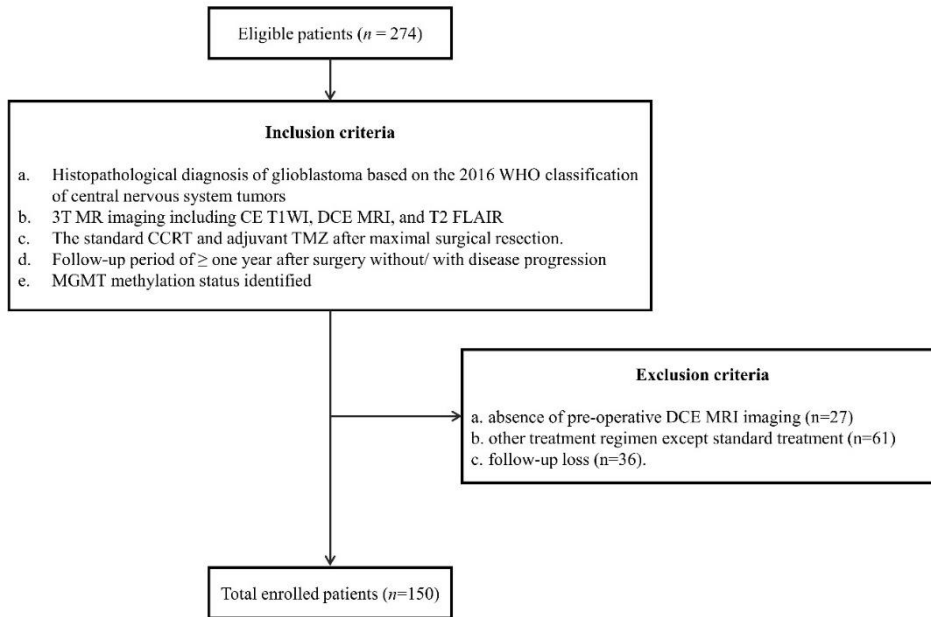


Figure 2. Inclusion/exclusion criteria for the study population.

Abbreviations: WHO, World Health Organization; DCE MRI, dynamic contrast-enhanced MRI; CE T1WI, contrast-enhanced T1-weighted imaging; T2 FLAIR, T2-weighted fluid attenuated inversion recovery; CCRT, concomitant chemoradiotherapy; MGMT, O6-methylguanine DNA methyltransferase; TMZ, temozolomide.

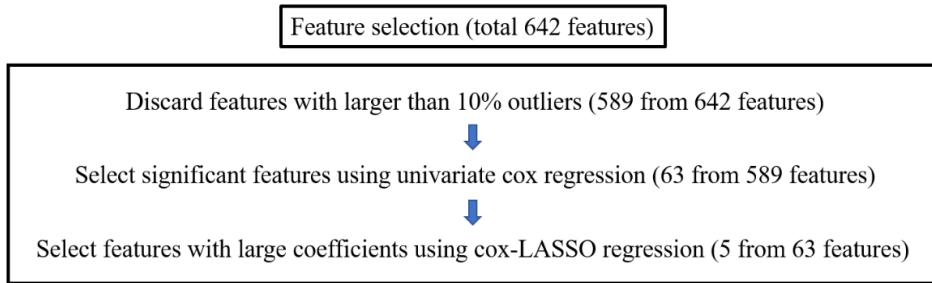


Figure 3. Illustration of the feature selection process

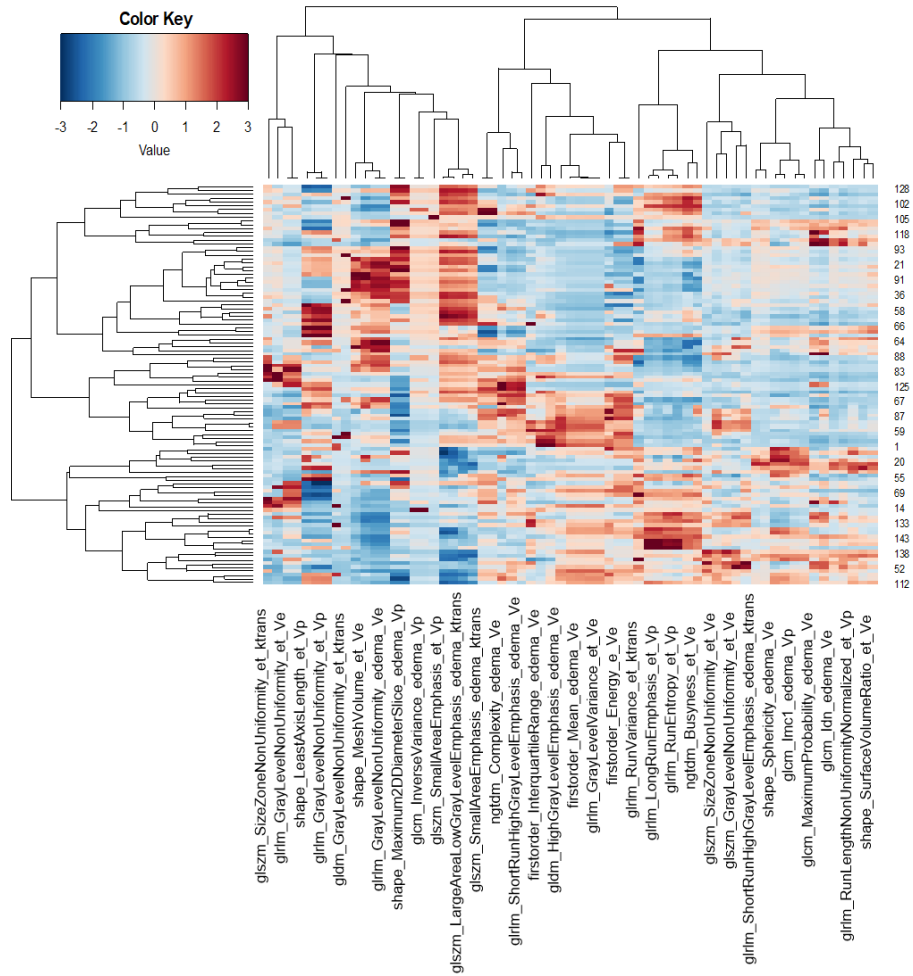


Figure 4. Heatmap of radiomic features using hierarchical clustering with dendrogram: for 63 selected features from univariate cox-regression

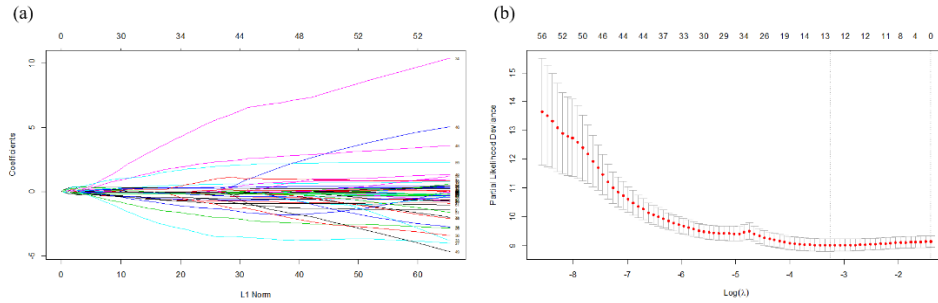


Figure 5. Intermediate results in the procedure of cox-LASSO model using training set: (a) plot of shrinkage of coefficients of regression variables. Note that large coefficients (vertical axis) reduced to around zero as L1 norm of total coefficients decreases (horizontal axis). (b) optimal λ value and a cross validated (CV) error plot to help evaluate the model. Note that the left vertical dot line shows us where the CV-error curve hits its minimum. The right vertical dot line shows us the most regularized model with CV-error within 1 standard deviation of the minimum. The *glmnet*, R package, gives the optimal number of reduced number of features (top horizontal axis).

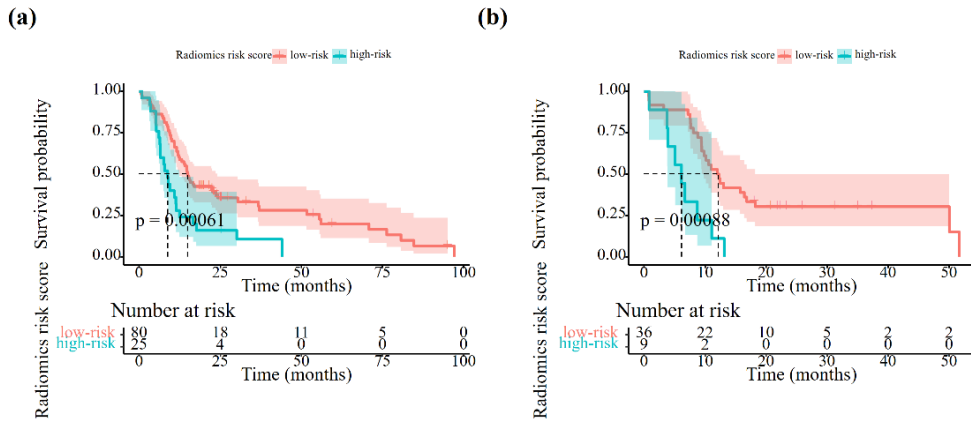


Figure 6. Risk group stratification using the radiomics score in the univariate Cox-regression model for predicting progress free survival: (a) discovery and (b) validation set, respectively.

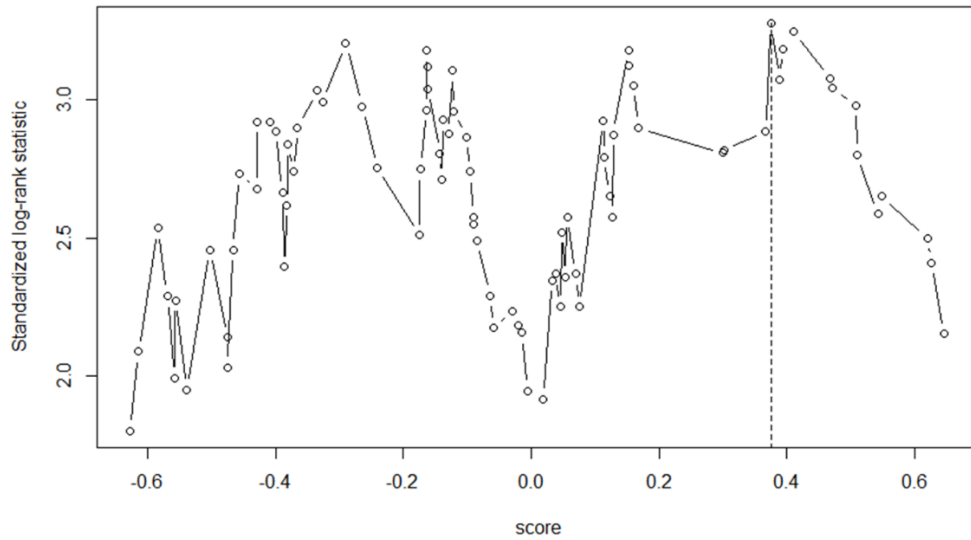


Figure 7. The intermediate result of calculating the cut-off value of the radiomics risk score obtained by maximally selected rank statistics using *maxstat* (R package): The cut-off value of was 0.374 ($M = 3.277$; $p = 0.017$).

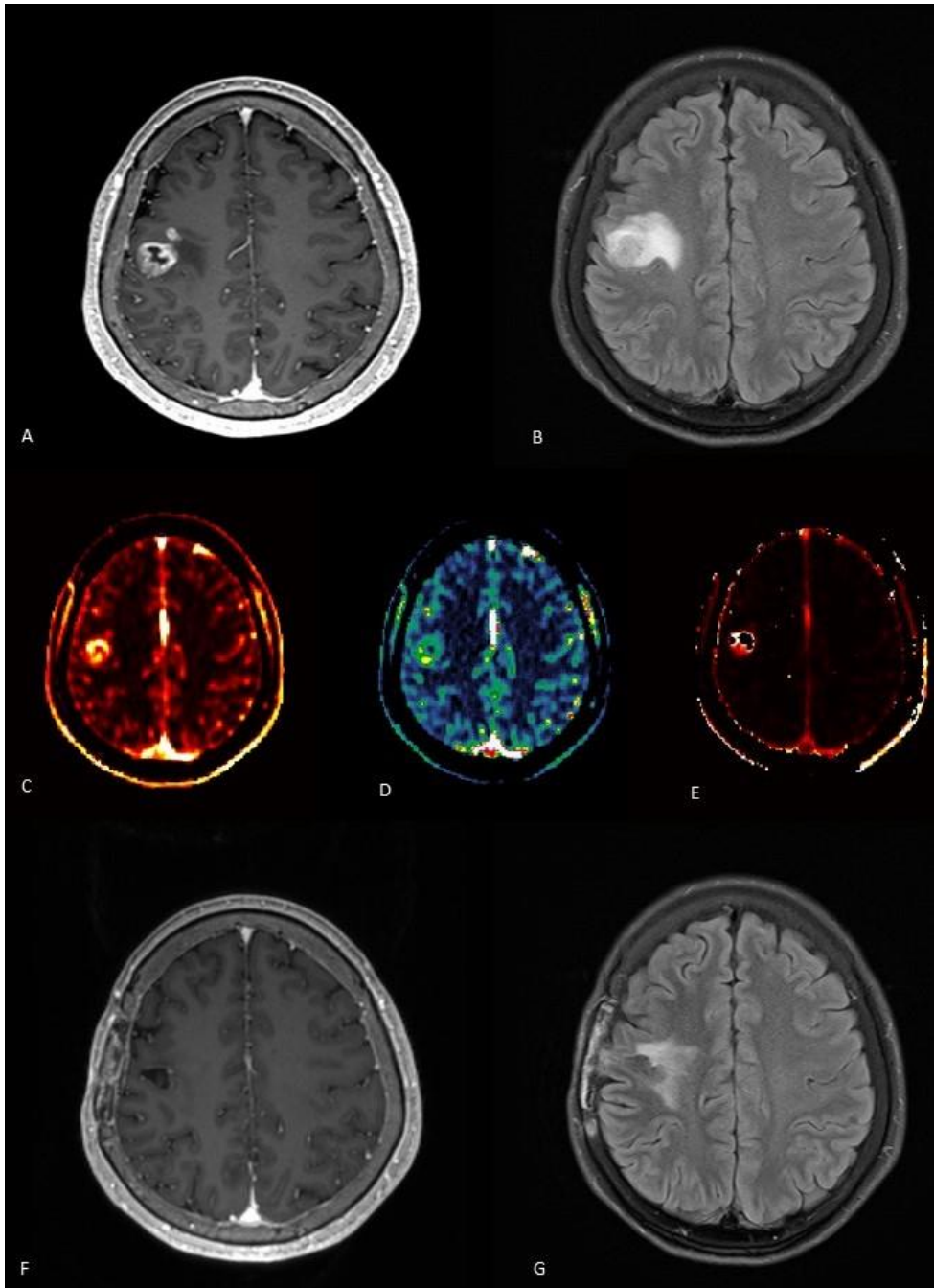


Figure 8. Low-risk patient (radiomics risk score: -0.9367459). A 51-year-old patient with glioblastoma. A preoperative axial MRI demonstrates a contrast-enhanced lesion with perilesional T2 high

signal intensity at the right frontal lobe: (A) Contrast-enhanced T1 weighted image; (B) FLAIR image; (C) K^{trans} ; (D) V_p ; and (E) V_e . Postoperative axial MRI at 1 year after operation demonstrates no new contrast-enhanced lesion (F) and (G).

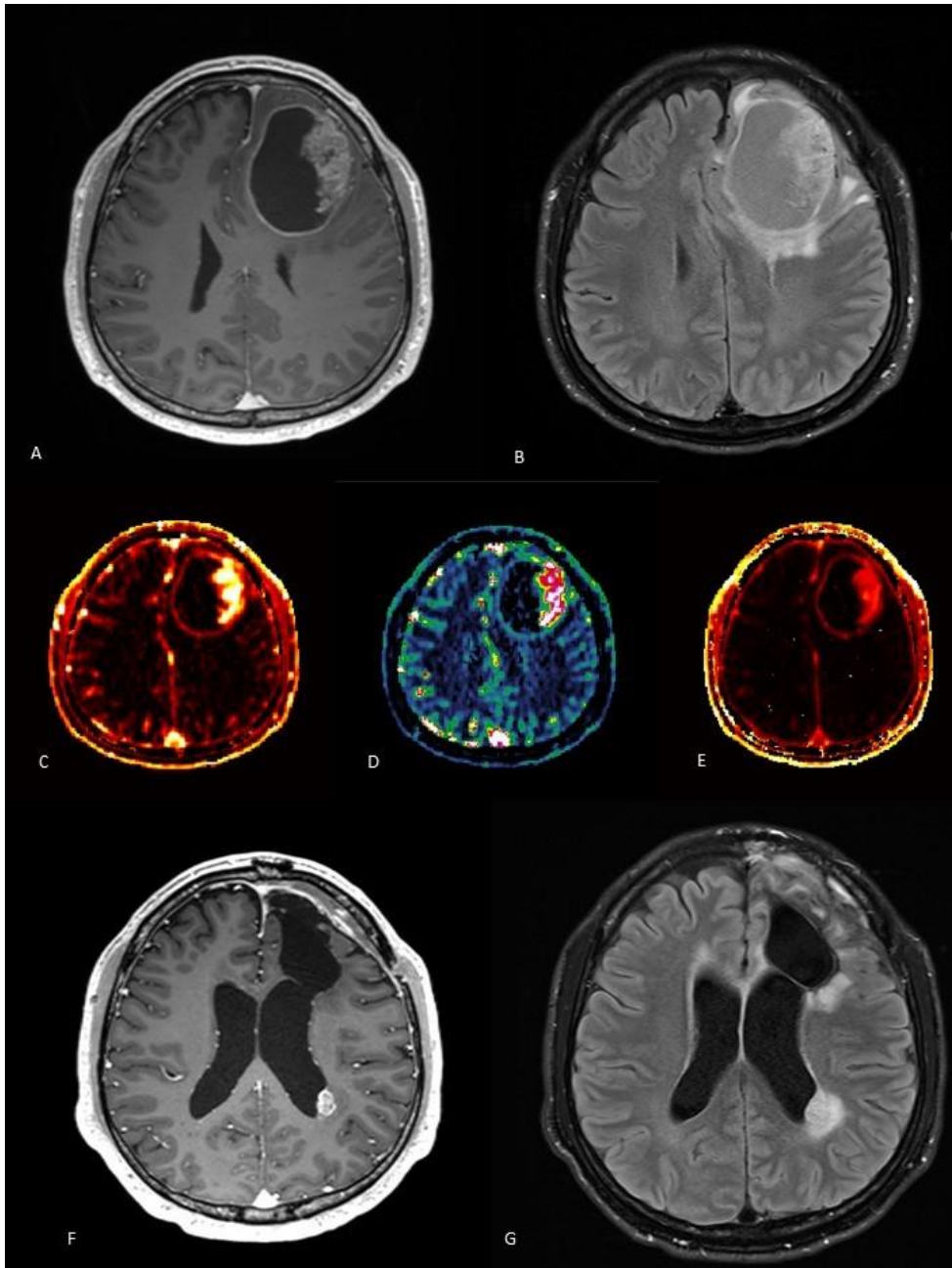


Figure 9. High-risk patient (radiomics risk score: 0.703891). A 43-year-old patient with glioblastoma. A preoperative axial MRI demonstrates a contrast-enhanced lesion with perilesional T2 high signal intensity at the left frontal lobe: (A) Contrast-enhanced T1

weighted image; (B) FLAIR image; (C) K^{trans} ; (D) V_p ; and (E) V_e . Postoperative axial MRI at 1 year after operation demonstrates a new contrast-enhanced lesion with T2 high signal intensity at the left lateral ventricle (F) and (G).

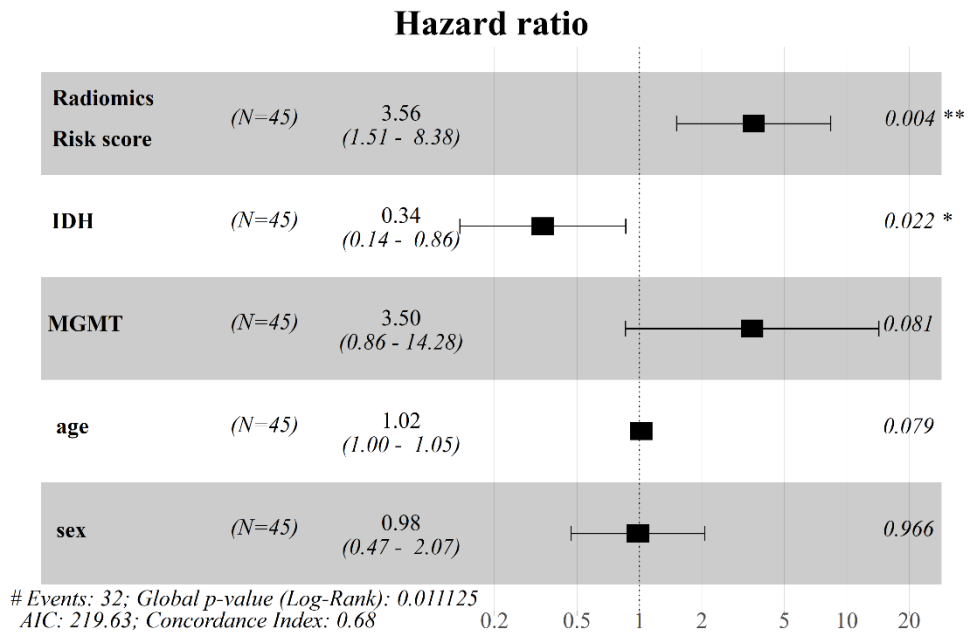


Figure 10. A forest plot for multivariate Cox proportional hazards model using clinical and radiomics variables.

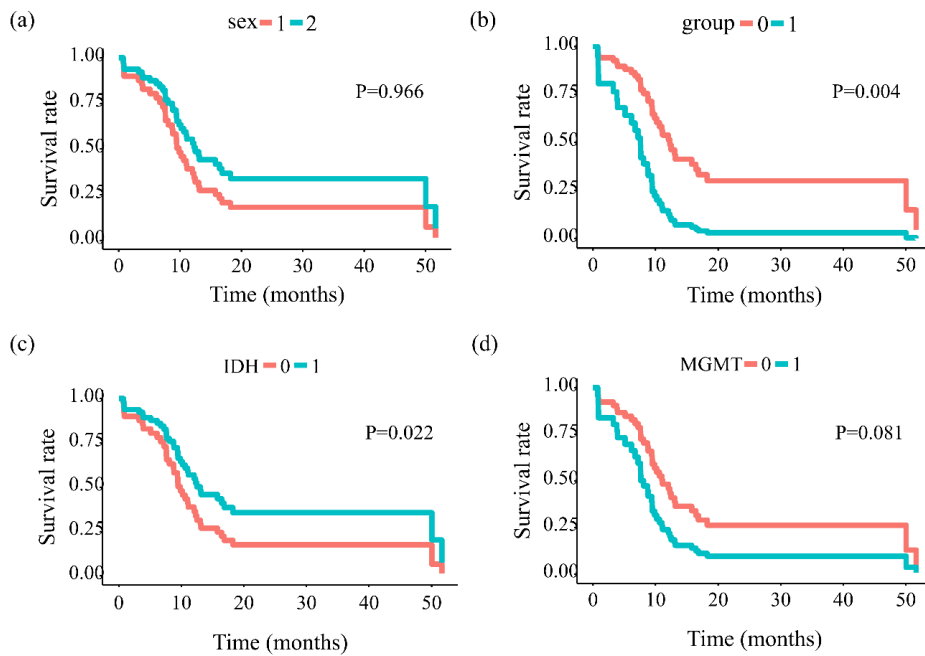


Figure 11. Survival curves of multivariate Cox–regression model for risk stratification using each variable of the validation set: (a) sex, (b) radiomics risk group, (c) IDH mutation status, and (d) MGMT methylation status.

Abbreviations: IDH, isocitrate dehydrogenase; MGMT, O6–methylguanine DNA methyltransferase.

Supplementary Materials

Radiomic Features

(<https://pyradiomics.readthedocs.io/en/latest/features.html#module-radiomics.shape>)

1. First-order features

The first-order features described the distribution of voxel intensities within the image region defined by the mask through commonly used and basic metrics.

Let X be a set of N_p voxels included in the ROI. $P(i)$ refers to the first order histogram with N_g discrete intensity levels, where N_g is the number of non-zero bins, equally spaced from 0 with a width defined in the binWidth parameter and $p(i)$ is the normalized first order histogram and equal to $\frac{P(i)}{N_p}$. ϵ is an arbitrarily small positive number ($\approx 2.2 \times 10^{-16} \approx 2.2 \times 10^{-16}$).

Energy	$\sum_{i=1}^{N_p} (X(i) + c)^2$	Interquartil e Range	$P_{75} - P_{25}$
Total energy y	$V_{\text{voxel}} \sum_{i=1}^{N_p} (X(i) + c)^2$	Range	$\max(X) - \min(X)$

Entropy	$-\sum_{i=1}^{N_g} p(i) \log_2(p(i)) + \epsilon)$	Mean absolute deviation (MAD)	$\frac{1}{N_p} \sum_{i=1}^{N_p} X(i) - \bar{X} $
Minimum	$\min(X)$	Robust Mean Absolute Deviation (rMAD)	$\frac{1}{N_{10-90}} \sum_{i=1}^{N_{10-90}} X_{10-90}(i) - \bar{X}_{10-90} $
10th percentile	The 10 th percentile of X	Root mean squared (RMS)	$\sqrt{\frac{1}{N_p} \sum_{i=1}^{N_p} (X(i) + c)^2}$
90th percentile	The 90 th percentile of X	Skewness	$\frac{\frac{1}{N_p} \sum_{i=1}^{N_p} (X(i) - \bar{X})^3}{\left(\sqrt{\frac{1}{N_p} \sum_{i=1}^{N_p} (X(i) - \bar{X})^2} \right)^3}$
Maximum	$\max(X)$	Kurtosis	$\frac{\frac{1}{N_p} \sum_{i=1}^{N_p} (X(i) - \bar{X})^4}{\left(\frac{1}{N_p} \sum_{i=1}^{N_p} (X(i) - \bar{X})^2 \right)^2}$
Mean	$\frac{1}{N_p} \sum_{i=1}^{N_p} X(i)$	Variance	$\frac{1}{N_p} \sum_{i=1}^{N_p} (X(i) - \bar{X})^2$
Median	The median gray-level intensity within	Uniformity	$\sum_{i=1}^{N_g} p(i)^2$

the ROI.

2. Shape features

Shape features included descriptors of the three-dimensional size and shape of the ROI. They are independent from the gray level intensity distribution in the ROI and were therefore only calculated on the non-derived image and mask.

Unless otherwise specified, features were derived from the approximated shape defined by the triangle mesh. To build this mesh, vertices (points) were first defined as points halfway on an edge between a voxel included in the ROI and one outside the ROI. By connecting these vertices a mesh of connected triangles was obtained, with each triangle defined by 3 adjacent vertices, which shared each side with exactly one other triangle.

This mesh was generated using a marching cubes algorithm. In this algorithm, a 2x2 cube was moved through the mask space. For each position, the corners of the cube were then marked ‘segmented’ (1) or ‘not segmented’ (0). Treating the corners

as specific bits in a binary number, a unique cube-index is obtained (0–255). This index was then used to determine which triangles were present in the cube.

These triangles were defined in such a way, that the normal (obtained from the cross product of vectors describing 2 out of 3 edges) were always oriented in the same direction.

Let N_v represent the number of voxels included in the ROI and N_f represent the number of faces (triangles) defining the Mesh. V is the volume of the mesh in mm^3 and A is the surface area of the mesh in mm^2 .

Elongation	$\sqrt{\frac{\lambda_{minor}}{\lambda_{major}}}$	Maximum 3 D diameter	The largest pairwise Euclidean distance between tumor surface mesh vertices.
Flatness	$\sqrt{\frac{\lambda_{least}}{\lambda_{major}}}$	Mesh volume	$V_i = \frac{O_{a_i} \cdot (O_{b_i} \times O_{c_i})}{6}$ $V = \sum_{i=1}^{N_f} V_i$
Least axis 1 length	$4\sqrt{\lambda_{least}}$	Minor axis 1 length	$4\sqrt{\lambda_{minor}}$

Major axis length	$4\sqrt{\lambda_{major}}$	Sphericity	$\frac{\sqrt[3]{36\pi V^2}}{A}$
Maximum 2D diameter (column)	The largest pairwise Euclidean distance between tumor surface mesh vertices in the row-column plane.	Surface area	$A_i = \frac{1}{2} a_i b_i \times a_i c_i $ $A = \sum_{i=1}^{N_f} A_i$
Maximum 2D diameter (row)	The largest pairwise Euclidean distance between tumor surface mesh vertices in the column-slice plane.	Surface area to volume ratio	$\frac{A}{V}$

Maximum 2 D diameter(slice)	The largest pairwise Euclidean distance between tumor surface mesh vertices in the row-slice plane.	Voxel volume	$V_{voxel} = \sum_{k=1}^{N_v} V_k$

3. Gray scale variation features

Gray scale variation features widely used in pattern recognition, refer to higher order statistical measures and summarize the local spatial arrangement of intensities.

3-1. Gray level co-occurrence matrix (GLCM) features

A Gray Level Co-occurrence Matrix (GLCM) of size $N_g \times N_g$ described the second-order joint probability function of an image region constrained by the mask and was defined as

$P(i, j | \delta, \theta)$. The $(i, j)^{th}$ element of this matrix represented the number of times the combination of levels i and j occurred in two pixels in the image, that were separated by a distance of δ pixels

along angle θ . The distance δ from the center voxel was defined as the distance according to the infinity norm. For $\delta = 1$, this resulted in 2 neighbors for each of 13 angles in 3D (26-connectivity) and for $\delta = 2$ a 98-connectivity (49 unique angles).

Let ϵ be an arbitrarily small positive number ($\approx 2.2 \times 10^{-16}$), $P(i, j)$ be the co-occurrence matrix for an arbitrary δ and θ , $p(i, j)$ be the normalized co-occurrence matrix and equal to $\frac{P(i, j)}{\sum P(i, j)}$, N_g be the number of discrete intensity levels in the image, $p_x(i) = \sum_{j=1}^{N_g} P(i, j)$ be the marginal row probabilities, $p_x(i) = \sum_{j=1}^{N_g} P(i, j)$ be the marginal column probabilities, μ_x be the mean gray level intensity of p_x and defined as $\mu_x = \sum_{i=1}^{N_g} p_x(i) i$, μ_y be the mean gray level intensity of p_y and defined as $\mu_y = \sum_{j=1}^{N_g} p_y(j) j$, σ_x be the standard deviation of p_x , σ_y be the standard deviation of p_y , $p_{x+y}(k) = \sum_{i=1}^{N_g} \sum_{j=1}^{N_g} p(i, j)$, where $i + j = k$, and $k = 2, 3, \dots, 2N_g$, $p_{x-y}(k) = \sum_{i=1}^{N_g} \sum_{j=1}^{N_g} p(i, j)$, where $|i - j| = k$, and $k = 0, 1, \dots, N_g - 1$, $HX = -\sum_{i=1}^{N_g} p_x(i) \log_2(p_x(i) + \epsilon)$ be the entropy of p_x , $HY = -\sum_{j=1}^{N_g} p_y(j) \log_2(p_y(j) + \epsilon)$ be the entropy of p_y , $HXY = -\sum_{i=1}^{N_g} \sum_{j=1}^{N_g} p(i, j) \log_2(p(i, j) + \epsilon)$ be the entropy of $p(i, j)$, $HXY1 = -\sum_{i=1}^{N_g} \sum_{j=1}^{N_g} p(i, j) \log_2(p_x(i)p_y(j) + \epsilon)$, and

$$\text{HXY2} = -\sum_{i=1}^{N_g} \sum_{j=1}^{N_g} p_x(i)p_y(j) \log_2(p_x(i)p_y(j) + \epsilon)$$

Autocorrelation	$\sum_{i=1}^{N_g} \sum_{j=1}^{N_g} p(i,j)ij$	Joint average	$\sum_{i=1}^{N_g} \sum_{j=1}^{N_g} p(i,j)i$
Cluster prominence	$\sum_{i=1}^{N_g} \sum_{j=1}^{N_g} (i+j-\mu_x - \mu_y)^4 p(i,j)$	Inverse difference (ID)	$\sum_{k=0}^{N_g-1} \frac{p_{x-y}(k)}{1+k}$
Cluster shade	$\sum_{i=1}^{N_g} \sum_{j=1}^{N_g} (i+j-\mu_x - \mu_y)^3 p(i,j)$	Inverse difference normalized (IDN)	$\sum_{k=0}^{N_g-1} \frac{p_{x-y}(k)}{1+\left(\frac{k}{N_g}\right)}$
Cluster tendency	$\sum_{i=1}^{N_g} \sum_{j=1}^{N_g} (i+j-\mu_x - \mu_y)^2 p(i,j)$	Inverse difference moment (IDM)	$\sum_{k=0}^{N_g-1} \frac{p_{x-y}(k)}{1+k^2}$
Contrast	$\sum_{i=1}^{N_g} \sum_{j=1}^{N_g} (i-j)^2 p(i,j)$	Inverse difference moment normalized (IDMN)	$\sum_{k=0}^{N_g-1} \frac{p_{x-y}(k)}{1+\left(\frac{k^2}{N_g^2}\right)}$
Correlation	$\frac{\sum_{i=1}^{N_g} \sum_{j=1}^{N_g} p(i,j)ij - \sigma_x(i)\sigma_y(i)}{\sigma_x(i)\sigma_y(i)}$	Inverse variance	$\sum_{k=1}^{N_g-1} \frac{p_{x-y}(k)}{k^2}$

Difference average	$\sum_{k=0}^{N_g-1} k p_{x-y}(k)$	Joint energy	$\sum_{i=1}^{N_g} \sum_{j=1}^{N_g} (p(i,j))^2$
Difference entropy	$\sum_{k=0}^{N_g-1} p_{x-y}(k) \log_2(p_{x-y}(k) + \epsilon)$	Joint entropy	$-\sum_{i=1}^{N_g} \sum_{j=1}^{N_g} p(i,j) \log_2(p(i,j) + \epsilon)$
Difference variance	$\sum_{k=0}^{N_g-1} (k - DA)^2 p_{x-y}(k)$	Maximum probability	$\max(p(i,j))$
Sum of squares	$\sum_{i=1}^{N_g} \sum_{j=1}^{N_g} (i - \mu_x)^2 p(i,j)$	Maximal correlation coefficient (MC C)	$\sqrt{\text{second largest eigenvalue of } Q}$ $Q(i,j)$ $= \sum_{k=0}^{N_g} \frac{p(i,k)p(j,k)}{p_x(i)p_y(k)}$
Sum average	$\sum_{k=2}^{2N_g} p_{x+y}(k) k$	Informational measure of correlation (I MC) 1	$\frac{HXY - HXY1}{\max\{HX, HY\}}$
Sum entropy	$\sum_{k=2}^{2N_g} p_{x+y}(k) \log_2 p_{x+y}(k) + \epsilon)$	Informational measure of correlation (I MC) 2	$\sqrt{1 - e^{-2(HXY2 - HXY)}}$

3-2. Gray level size zone matrix (GLSZM) features

A Gray Level Size Zone (GLSZM) quantified gray level zones in an image. A gray level zone was defined as the number of connected voxels that shared the same gray level intensity. A voxel was considered connected if the distance was 1 according to the infinity norm (26-connected region in a 3D, 8-connected region in 2D). In a gray level size zone matrix $p(i, j)$, the $(i, j)^{th}$ element equaled the number of zones with gray level i and size j appeared in image. Contrary to GLCM and GLRLM, the GLSZM was rotation independent, with only one matrix calculated for all directions in the ROI.

Let N_g be the number of discrete intensity values in the image, N_s be the number of discrete zone sizes in the image, N_p be the number of voxels in the image, N_z be the number of zones in the ROI, which is equal to $\sum_{i=1}^{N_g} \sum_{j=1}^{N_g} P(i, j)$ and $1 \leq N_z \leq N_p$, $P(i, j)$ be the size zone matrix, and $p(i, j)$ be the normalized size zone matrix, defined as $p(i, j) = \frac{P(i, j)}{N_z}$

Small area		Zone	$\sum_{i=1}^{N_g} \sum_{j=1}^{N_g} p(i, j) (j$
emphasis (SA	$\frac{\sum_{i=1}^{N_g} \sum_{j=1}^{N_s} \frac{P(i, j)}{j^2}}{N_z}$	variance (ZV	$-\mu)^2,$
E))	$\mu = \sum_{i=1}^{N_g} \sum_{j=1}^{N_g} p(i, j) j$
Large area		Zone	$-\sum_{i=1}^{N_g} \sum_{j=1}^{N_s} p(i, j) \log$
emphasis (LA	$\frac{\sum_{i=1}^{N_g} \sum_{j=1}^{N_s} P(i, j) j^2}{N_z}$	entropy (ZE)	$\epsilon)$
E)			
Gray level		Low gray	
non-		level zone	
uniformity (GL	$\frac{\sum_{i=1}^{N_g} (\sum_{j=1}^{N_s} P(i, j))}{N_z}$	emphasis (LG	$\frac{\sum_{i=1}^{N_g} \sum_{j=1}^{N_s} \frac{P(i, j)}{i^2}}{N_z}$
N)		LZE)	
Gray level		High gray	
non-		level zone	
uniformity	$\frac{\sum_{i=1}^{N_g} (\sum_{j=1}^{N_s} P(i, j))}{N_z^2}$	emphasis (HG	$\frac{\sum_{i=1}^{N_g} \sum_{j=1}^{N_s} P(i, j) i^2}{N_z}$
normalized (G		LZE)	
LNN)			

Size-zone		Small area	
non-		low gray level	
uniformity (SZ	$\frac{\sum_{j=1}^{N_s} \left(\sum_{i=1}^{N_g} P(i, j) \right)}{N_z}$	emphasis (SAL	$\frac{\sum_{i=1}^{N_g} \sum_{j=1}^{N_s} \frac{P(i, j)}{i^2 j^2}}{N_z}$
N)		GLE)	
Size-zone		Small area high	
non-		gray level	
uniformity	$\frac{\sum_{j=1}^{N_s} \left(\sum_{i=1}^{N_g} P(i, j) \right)}{N_z^2}$	emphasis (SAH	$\frac{\sum_{i=1}^{N_g} \sum_{j=1}^{N_s} \frac{P(i, j) i^2}{j^2}}{N_z}$
normalized (SZ		GLE)	
NN)			
Zone		Large area low	
percentage (Z	$\frac{N_z}{N_p}$	gray level	
P)		emphasis (LAL	$\frac{\sum_{i=1}^{N_g} \sum_{j=1}^{N_s} \frac{P(i, j) j^2}{i^2}}{N_z}$
		GLE)	
Gray level	$\sum_{i=1}^{N_g} \sum_{j=1}^{N_s} p(i, j) (i$	Large area high	
variance (GLV	$-\mu)^2,$	gray level	
)	μ	emphasis (LAH	$\frac{\sum_{i=1}^{N_g} \sum_{j=1}^{N_s} P(i, j) i^2 j^2}{N_z}$
	$= \sum_{i=1}^{N_g} \sum_{j=1}^{N_s} p(i, j) i$	GLE)	

3-3. Gray level run length matrix (GLRLM) features

A Gray Level Run Length Matrix (GLRLM) quantified gray level runs, which were defined as the length in number of pixels, of consecutive pixels that had the same gray level value. In a gray level run length matrix $P(i, j|\theta)$, the $(i, j)^{th}$ element described the number of runs with gray level i and length j occurred in the image (ROI) along angle θ .

Let N_g be the number of discrete intensity values in the image, N_s be the number of discrete zone sizes in the image, N_r be the number of discrete run lengths in the image, N_p be the number of voxels in the image, $N_r(\theta)$ be the number of runs in the image along angle θ , which is equal to $\sum_{i=1}^{N_g} \sum_{j=1}^{N_g} P(i, j|\theta)$ and $1 \leq N_r(\theta) \leq N_p$, $P(i, j|\theta)$ be the run length matrix for an arbitrary direction θ , and $p(i, j|\theta)$ be the normalized run length matrix, defined as $p(i, j|\theta) = \frac{P(i, j|\theta)}{N_r(\theta)}$.

Short run		Run	$\sum_{i=1}^{N_g} \sum_{j=1}^{N_r} p(i, j \theta)j$
emphasis (SRE	$\frac{\sum_{i=1}^{N_g} \sum_{j=1}^{N_r} \frac{P(i, j \theta)}{j^2}}{N_r(\theta)}$	variance (RV	$-\mu^2$,
))		$\mu = \sum_{i=1}^{N_g} \sum_{j=1}^{N_r} p(i, j \theta)j$

Long run emphasis (LRE)	$\frac{\sum_{i=1}^{N_g} \sum_{j=1}^{N_r} P(i, j \theta)}{N_r(\theta)}$	Run entropy (RE)	$-\sum_{i=1}^{N_g} \sum_{j=1}^{N_r} p(i, j \theta) \log(\epsilon)$
Gray level non- uniformity (GL N)	$\frac{\sum_{i=1}^{N_g} \left(\sum_{j=1}^{N_r} P(i, j \theta) \right)}{N_r(\theta)}$	Low gray level run emphasis (LG LRE)	$\frac{\sum_{i=1}^{N_g} \sum_{j=1}^{N_r} \frac{P(i, j \theta)}{i^2}}{N_r(\theta)}$
Gray level non- uniformity normalized (GL NN)	$\frac{\sum_{i=1}^{N_g} \left(\sum_{j=1}^{N_r} P(i, j \theta) \right)}{N_r(\theta)^2}$	High gray level run emphasis (HG LRE)	$\frac{\sum_{i=1}^{N_g} \sum_{j=1}^{N_r} P(i, j \theta) i^2}{N_r(\theta)}$
Run length non- uniformity (RL N)	$\frac{\sum_{j=1}^{N_r} \left(\sum_{i=1}^{N_g} P(i, j \theta) \right)}{N_r(\theta)}$	Short run low gray level emphasis (SRL GLE)	$\frac{\sum_{i=1}^{N_g} \sum_{j=1}^{N_r} \frac{P(i, j \theta)}{i^2 j^2}}{N_r(\theta)}$
Run length non- uniformity normalized (RL)	$\frac{\sum_{j=1}^{N_r} \left(\sum_{i=1}^{N_g} P(i, j \theta) \right)}{N_r(\theta)^2}$	Short run high gray level emphasis (SRH GLE)	$\frac{\sum_{i=1}^{N_g} \sum_{j=1}^{N_r} \frac{P(i, j \theta) i^2}{j^2}}{N_z}$

NN)

			Long run low
Run			gray level
percentage (R	$\frac{N_r(\theta)}{N_p}$		$\frac{\sum_{i=1}^{N_g} \sum_{j=1}^{N_r} \frac{P(i, j \theta)j^2}{i^2}}{N_r(\theta)}$
P)		emphasis (LRL	GRE)

	$\sum_{i=1}^{N_g} \sum_{j=1}^{N_r} p(i, j \theta)(i$		Long run high
Gray level	$-\mu)^2,$		gray level
variance (GLV	μ		$\frac{\sum_{i=1}^{N_g} \sum_{j=1}^{N_r} P(i, j \theta)i^2j^2}{N_r(\theta)}$
)	$= \sum_{i=1}^{N_g} \sum_{j=1}^{N_r} p(i, j \theta)i$	emphasis (LRH	GLE)

3-4. Neighboring gray tone difference matrix (NGTDM)

features

A Neighboring Gray Tone Difference Matrix (NGTDM) quantified the difference between a gray value and the average gray value of its neighbors within distance δ . The sum of absolute differences for

gray level i was stored in the matrix.

Let X_{gl} be a set of segmented voxels and $x_{gl}(j_x, j_y, j_z) \in X_{gl}$ be the gray level of a voxel at position (j_x, j_y, j_z) , then the average gray level of the neighborhood is:

$$\bar{A}_i = \bar{A}(j_x, j_y, j_z) = \frac{1}{W} \sum_{k_x=-\delta}^{\delta} \sum_{k_y=-\delta}^{\delta} \sum_{k_z=-\delta}^{\delta} x_{gl}(j_x + k_x, j_y + k_y, j_z + k_z),$$

where $(k_x, k_y, k_z) \neq (0, 0, 0)$ and $x_{gl}(j_x + k_x, j_y + k_y, j_z + k_z) \in X_{gl}$

W is the number of voxels in the neighborhood that are also in X_{gl} .

Let n_i be the number of voxels in X_{gl} with gray level i , $N_{v,p}$ be the total number of voxels in X_{gl} and equal to $\sum n_i$ (i.e. the number of voxels with a valid region; at least 1 neighbor). $N_{v,p} \leq N_p$, where N_p is the total number of voxels in the ROI, p_i be the gray level probability

and equal to n_i / N_v , $s_i = \begin{cases} \sum n_i |i - \bar{A}_i| & \text{for } n_i \neq 0 \\ 0 & \text{for } n_i = 0 \end{cases}$ be the sum of

absolute differences for gray level i , N_g be the number of discrete gray levels, and $N_{g,p}$ be the number of gray levels where $p_i \neq 0$.

Coars	$\frac{1}{\sum_{i=1}^{N_g} p_i s_i}$	Complexi	$\frac{1}{N_{v,p}} \sum_{i=1}^{N_g} \sum_{j=1}^{N_g} i - j \frac{p_i s_i + p_j s_j}{p_i + p_j}$,
eness		ty	where $p_i \neq 0, p_j \neq 0$

Busyness	$\frac{\sum_{i=1}^{N_g} p_i s_i}{\sum_{i=1}^{N_g} \sum_{j=1}^{N_g} ip_i - jp_j },$	Strength	$\frac{\sum_{i=1}^{N_g} \sum_{j=1}^{N_g} (p_i + p_j)(i-j)^2}{\sum_{i=1}^{N_g} s_i},$
	where $p_i \neq 0, p_j \neq 0$		where $p_i \neq 0, p_j \neq 0$
Contrast	$\left(\frac{1}{N_{g,p}(N_{g,p}-1)} \sum_{i=1}^{N_g} \sum_{j=1}^{N_g} p_i p_j (i-j)^2 \right) \left(\frac{1}{N_{v,p}} \sum_{i=1}^{N_g} s_i \right),$		
	where $p_i \neq 0, p_j \neq 0$		

3–5. Gray level dependence matrix (GLDM) features

A Gray Level Dependence Matrix (GLDM) quantified gray level dependencies in an image. A gray level dependency was defined as the number of connected voxels within distance δ that are dependent on the center voxel. A neighboring voxel with gray level j was considered dependent on center voxel with gray level i if $|i - j| \leq \alpha$. In a gray level dependence matrix $P(i, j)$, the $(i, j)^{th}$ element described the number of times a voxel with gray level i with j dependent voxels in its neighborhood appears in image.

Let N_g be the number of discrete intensity values in the image, N_d be the number of discrete dependency sizes in the image, N_z be the number of dependency zones in the image, which is equal to $\sum_{i=1}^{N_g} \sum_{j=1}^{N_d} P(i, j)$, $P(i, j)$ be the dependence matrix, and $p(i, j)$ be the

normalized dependence matrix, defined as $p(i, j) = \frac{P(i, j)}{N_z}$

Small			
dependenc		Dependence	$\sum_{i=1}^{N_g} \sum_{j=1}^{N_d} p(i, j)(j - \mu)^2,$
e	$\frac{\sum_{i=1}^{N_g} \sum_{j=1}^{N_d} \frac{P(i, j)}{i^2}}{N_z}$	variance (D	$\mu = \frac{\sum_{i=1}^{N_g} \sum_{j=1}^{N_d} p(i, j)j}{\sum_{i=1}^{N_g} \sum_{j=1}^{N_d} p(i, j)}$
emphasis (V)	
SDE)			
Large		Low gray	
dependenc		level	
e	$\frac{\sum_{i=1}^{N_g} \sum_{j=1}^{N_d} P(i, j)j^2}{N_z}$	emphasis (LG	$\frac{\sum_{i=1}^{N_g} \sum_{j=1}^{N_d} \frac{P(i, j)}{i^2}}{N_z}$
emphasis (LE)	
LDE)			
Gray level		High gray	
non-		level	
uniformity (G	$\frac{\sum_{i=1}^{N_g} \left(\sum_{j=1}^{N_d} P(i, j) \right)}{N_z}$	emphasis (HG	$\frac{\sum_{i=1}^{N_g} \sum_{j=1}^{N_d} P(i, j)i^2}{N_z}$
LN)		LE)	
Dependenc		Small	
e non-		dependence	
uniformity ($\frac{\sum_{j=1}^{N_d} \left(\sum_{i=1}^{N_g} P(i, j) \right)}{N_z}$	low gray level	$\frac{\sum_{i=1}^{N_g} \sum_{j=1}^{N_d} \frac{P(i, j)}{i^2 j^2}}{N_z}$
DN)		emphasis (SD	
		LGLE)	

Dependence		Small	The joint
non-		dependence	distribution of small
uniformity	$\frac{\sum_{j=1}^{N_d} \left(\sum_{i=1}^{N_g} P(i,j) \right)}{N_z^2}$	high gray level	dependence with
normalized(D		emphasis(SD	higher gray-level
NN)		HGLE)	values.

Dependence		Large	
e	$-\sum_{i=1}^{N_g} \sum_{j=1}^{N_d} p(i,j)$	dependence	
entropy (D	$\epsilon)$	high gray level	$\frac{\sum_{i=1}^{N_g} \sum_{j=1}^{N_d} P(i,j) i^2 j^2}{N_z}$
E)		emphasis(LDH	
		GLE)	
	$\sum_{i=1}^{N_g} \sum_{j=1}^{N_d} p(i,j) i$	Large	
Gray level	$-\mu)^2,$	dependence	
variance (G	μ	low gray level	$\frac{\sum_{i=1}^{N_g} \sum_{j=1}^{N_d} \frac{P(i,j) j^2}{i^2}}{N_z}$
LV)	$= \sum_{i=1}^{N_g} \sum_{j=1}^{N_d} p(i,j) i$	emphasis(LDL	
		GLE)	

국문 초록

교모세포종 환자에서의 역동적 조영증강 자기공명영상의 라디오믹스 점수를 이용한 IDH 돌연변이 상태 독립적 고위험군 예측 연구

서울대학교 대학원

의학과 영상의학전공

박엘레나

목적: 본 연구의 목적은 교모세포종 환자의 고위험군을 예측하기 위해서 역동적 조영증강 자기공명영상 기반의 라디오믹스 점수를 개발하는 것이다.

방법: 본 연구에는 수술 전 DCE MRI를 시행받은 교모세포종 환자 150명 (남성 92명 (61.3%), 평균 연령 60.5 ± 13.5세)이 포함되었다. DCE MRI의 K^{trans} , V_p 및 V_e 지도 각각에서 640개의 radiomics 지표가 추출되었으며, 이를 위하여 종양 부위는 조영증강 T1WI와 FLAIR 영상을 이용하여 segmentation 하였다. 지표 선택 알고리즘을 사용하여 642개 지표 중 예후 예측에 특이적인 radiomics 지표를 선택했다. 다음으로, discovery set (n = 105)에서 선택된 지표의 가중치 조합을 사용하여 radiomics risk score를 개발하고 radiomics risk score에 기반하여 고위험 및 저위험 그룹 간의 예후 차이를 조사하여 validation set

(n = 45)에서 검증하였다. 마지막으로, 1년 무진행 생존을 분석을 위한 다변량 Cox- 회귀 기법을 사용하여 임상 변수와 함께 radiomics risk score의 예후 예측력을 평가하였다.

결과: 비조영증강 T2 고신호 영역에서 얻은 16 가지 radiomics 지표가 642개 지표 중 선택되었다. 이 두가지 지표를 이용하여 Radiomics risk score를 만들었으며, 이를 이용하였을 때, 로그 순위 테스트에서 discovery 및 test set에서 고위험군과 저 위험군을 유의미하게 구분할 수 있었다 ($p < 0.001$). Radiomics risk score는 isocitrate dehydrogenase (IDH) 돌연변이와 독립적인 예후 예측인자였다 (Hazard ratio (HR) = 3.56 ($p = 0.004$)).

결론: 교모세포종 환자에서 1년 무진행 생존을 예측에 있어 비조영증강 T2 고신호 영역에서의 DCE MRI 기반의 radiomics risk score 가 우수한 성적을 보였으며, 향후 이를 이용한 임상 이용 가능성이 기대된다.

.....

주요어 : 교모세포종, 라디오믹스, 역동적 조영증강 자기공명영상, K^{trans} , V_e , V_p

학 번: 2018-39720